



# High-performance rechargeable metal–air batteries enabled by efficient charge transport in multielement random alloy electrocatalyst

Chandran Balamurugan<sup>a,b</sup>, Changhoon Lee<sup>c,k</sup>, Kyusang Cho<sup>d</sup>, Jehan Kim<sup>e</sup>, Byoungwook Park<sup>f</sup>, Woochul Kim<sup>g</sup>, Namsoo Lim<sup>g</sup>, Hyeonhuh Kim<sup>h</sup>, Yusin Pak<sup>g</sup>, Keun Hwa Chae<sup>i</sup>, Ji Hoon Shim<sup>j,k</sup>, Sooncheol Kwon<sup>a,\*</sup>

<sup>a</sup> Department of Energy and Materials Engineering, Dongguk University-Seoul, Seoul 04620 Republic of Korea

<sup>b</sup> Heeger Center for Advanced Materials (HCAM), Gwangju Institute of Science and Technology (GIST), Gwangju 500-712, Republic of Korea

<sup>c</sup> Max Planck POSTECH Center for Complex Phase of Materials, Pohang University of Science and Technology, Pohang 37673, Republic of Korea

<sup>d</sup> Research Institute for Solar and Sustainable Energies (RISE), Gwangju Institute of Science and Technology (GIST), Gwangju 500-712, Republic of Korea

<sup>e</sup> Pohang Accelerator Laboratory, Pohang University of Science and Technology, Pohang 37673, Republic of Korea

<sup>f</sup> Division of Advanced Materials, Korea Research Institute of Chemical Technology, Daejeon 305-600, Republic of Korea

<sup>g</sup> Sensor System Research Center (SSRC), Korea Institute of Science and Technology (KIST), Seoul 02792, Republic of Korea

<sup>h</sup> Ceramic Total Solution Center, Korea Institute of Ceramic Engineering and Technology, Icheon, Gyeonggi 17303 Republic of Korea

<sup>i</sup> Advanced Analysis and Data Center, Korea Institute of Science and Technology, Seoul 02792, Republic of Korea

<sup>j</sup> Department of Chemistry, Pohang University of Science and Technology, Pohang 37673, Republic of Korea

<sup>k</sup> Division of Advanced Materials Science, Pohang University of Science and Technology, Pohang 37673, Republic of Korea

## ARTICLE INFO

### Keywords:

Virtual crystal approximation  
Multielement random alloy catalyst  
Electrocatalyst  
Oxygen electrolysis  
Energy storage  
Rechargeable metal–air pouch cell

## ABSTRACT

The integration of bifunctionally active sites of multielement random alloy catalysts with other metal oxide electrocatalysts is a promising strategy for efficient electrochemical reactions. In this study, a novel combination of virtual crystal approximation and hydrothermal synthesis was used to investigate the composition-dependent structure and electrical property in a  $\text{Ag}_{1-x}\text{Ni}_x$  catalyst. The combination showed that a hexagonal closed-packed structure of  $\text{Ag}_{1-x}\text{Ni}_x$  with a compositional ratio of 6:4 (Ag:Ni) had electrical conductivity of  $\sim 2 \times 10^7 \text{ S}\cdot\text{cm}^{-1}$  and an ionization potential of  $-5.4 \text{ eV}$ . Furthermore, the bifunctional oxygen electrocatalytic efficiencies of  $\text{Ag}_{0.6}\text{Ni}_{0.4}$  were improved by forming a heterointerface with the  $\text{CoNb}_2\text{O}_6$  electrocatalyst, resulting in a discharge-charge voltage gap of 0.81 V over 587 h, peak power density of  $178.9 \text{ mW}\cdot\text{cm}^{-2}$ , and specific capacity of  $806.8 \text{ mA}\cdot\text{h}\cdot\text{g}^{-1}$  in a zinc–air battery. This approach was applied to pouch-type zinc–air batteries, resulting in long-term stability of over 158.6 h at  $10 \text{ mA}\cdot\text{cm}^{-2}$ .

## 1. Introduction

An increasing demand for efficient electrochemical energy storage and conversion system in modern society has stimulated the development of novel rechargeable batteries that can realize the portable electronic revolution, in which highly sophisticated portable devices such as drones are widely and intensively utilized [1–5]. Rather than using conventional lithium-ion batteries that catch fire and explode, the emerging metal–air batteries in particular have been gaining increasing attention as they have the potential to contribute to the development of sustainable electrochemical energy and storage systems due to their high energy density and enhanced environmental friendliness [6,7]. For

example, rechargeable zinc–air batteries (ZABs) have the potential to provide four times more energy ( $1086 \text{ Wh kg}^{-1}$ ) in a sustainable and environmentally friendly manner than the most advanced lithium-ion batteries [8–14]. Additionally, the ZABs utilize a two-electrode system consisting of a catalytic air cathode and a nonprecious zinc anode, which significantly reduces the anthropological cost of these batteries [7, 15–17]. However, practical challenges in zinc–air batteries, such as low cycle life, poor reversibility, and low energy conversion efficiency [18–20], persist because of higher energy barriers, including the slow kinetics in the electrocatalytic oxygen reduction reaction (ORR) and oxygen evolution reaction (OER), and poor electrochemical durability in alkaline electrolytes [21,22].

\* Corresponding author.

E-mail address: [kwansc12@dongguk.edu](mailto:kwansc12@dongguk.edu) (S. Kwon).

<https://doi.org/10.1016/j.apcatb.2023.122631>

Received 26 November 2022; Received in revised form 14 February 2023; Accepted 12 March 2023

Available online 14 March 2023

0926-3373/© 2023 The Authors. Published by Elsevier B.V. This is an open access article under the CC BY-NC-ND license (<http://creativecommons.org/licenses/by-nc-nd/4.0/>).

For the improved bifunctional activity of electrocatalysts in ZABs, precious metals (e.g., Pt-based for ORR and Ir–Ru-based for OER) [23–25] and their corresponding oxides ( $\text{IrO}_2$  and  $\text{RuO}_2$ ) have typically been studied as the catalytic air cathode that uses molecular oxygen as fuel for the electrocatalytic reaction [26,27]. Alternatively, nonprecious metals (i.e., Fe, Co, and Ni), transition-metal composites (oxides, nitrides, and phosphides), and metal-supported carbon-based hybridization materials have also been investigated [28–32]. However, the long-term operation of these single metals and metal oxide-based composite catalysts is characterized by an inherent low conductivity and rapid deactivation of metal sites, resulting in an unbalanced symmetry of OER and ORR [33–35].

To address the aforementioned issues, intensive research has been conducted on the development of heterogeneous electrocatalysts containing both OER and ORR elements [15,36]. Accordingly, multielement random alloy (MRA) catalysts, in which more than one metal elements are randomly mixed together to produce high-tech metal materials with modified crystal and electronic structure, have been considered for the desirable bifunctionality in active catalysts owing to their high conductivity, surface area, and selective active sites [37–45]. In particular, the electrocatalytic features of MRA can be further extended when it change the chemical composition (i.e., mixing ratio of each component), which give a rise to the resultant crystal structure to determine a stability of active metal particles and a charge distribution with internal resistance. Unfortunately, however, predicting the desirable crystal structure and relevant electrocatalytic properties of MRA depending on the metal composition have not been investigated yet due to the thermodynamic complex of each component. In parallel, sophisticated control of metal composition and crystal structure of MRA during the fabrication are also required to ensure their electrochemical catalytic properties for the efficient rechargeable zinc-air batteries. In addition, the electrocatalytic properties of MRA can be enhanced further by coupling with a metal oxide-based electrocatalyst. Because, the integrating MRA into metal oxide system and building a new multi-component dual-phase (MRA/metal oxide) electrocatalyst with different heterointerface can induce a synergistic effect between various metals as well as expose more active sites and efficient charge transfer/redistribution, resulting in a high symmetry of OER and ORR, providing superior electrocatalytic performance [46,47]. Unfortunately, the electrical properties and durability of dual-phase electrocatalysts continue to lag behind commercialization due to a lack of knowledge of their composition–structure–transport relationship.

Herein, we report a novel dual-phase electrocatalyst comprised of AgNi random alloy and  $\text{CoNb}_2\text{O}_6$  nanocube as the bifunctional multi-component system derived using a sequential hydrothermal synthesis. By employing virtual crystal approximation (VCA), the optimal composition design and crystal structure of AgNi can be determined to have a specific atomic ratio of 6:4 (Ag:Ni) and a hexagonal closed-packed (*hcp*) structure, resulting in the highest electrical conductivity ( $\sigma \sim 2 \times 10^7 \text{ Scm}^{-1}$ ) and ionized potential ( $\sim -5.4 \text{ eV}$ ). Based on this information, we have successfully fabricated  $\text{Ag}_{0.6}\text{Ni}_{0.4}$  electrocatalysts that are distributed on top of  $\text{CoNb}_2\text{O}_6$  nanocubic electrocatalysts via a sequential hydrothermal process, allowing sophisticated control of chemical composition. The resultant dual-phase  $\text{CoNb}_2\text{O}_6 @ \text{Ag}_{0.6}\text{Ni}_{0.4}$  offers a high surface-to-volume ratio, exposed active sites and defect-enriched surface, thereby enhancing the OER/ORR bifunctional activity and charge transports. The  $\text{CoNb}_2\text{O}_6 @ \text{Ag}_{0.6}\text{Ni}_{0.4}$  catalyst exhibits outstanding electrochemical activity ( $E_j = 10 \text{ (OER)} - E_{1/2} \text{ (ORR)} = 0.49 \text{ V}$ ) and excellent ORR and OER cycle durability. Furthermore, the dual-phase  $\text{CoNb}_2\text{O}_6 @ \text{Ag}_{0.6}\text{Ni}_{0.4}$  catalysts are directly applied as an air cathode for zinc–air batteries, providing a stable discharge/charge voltage gap of 0.81 V over 587 h at a current density of  $10 \text{ mAcm}^{-2}$ , also delivers excellent peak power density ( $178.9 \text{ mW cm}^{-2}$  at  $213 \text{ mA cm}^{-2}$ ) and specific capacity ( $806.8 \text{ mA h g}^{-1}$ ). From a practical perspective, we also designed pouch-type zinc–air batteries using  $\text{CoNb}_2\text{O}_6 @ \text{Ag}_{0.6}\text{Ni}_{0.4}$  catalysts as the air cathode, which exhibit an excellent rate capability,

peak power density ( $135.6 \text{ mW cm}^{-2}$  at  $150 \text{ mA cm}^{-2}$ ) and long-term stability for more than 158.6 h at a current density of  $10 \text{ mA cm}^{-2}$ .

## 2. Experimental

### 2.1. Estimation of electrical and electronic properties of $\text{Ag}_{1-x}\text{Ni}_x$ using VCA

Through density functional theory (DFT), we initially examined the electronic structural and electric transport properties of  $\text{Ag}_{1-x}\text{Ni}_x$  random alloy as a function of Ag content for *hcp* and *fcc* structures.  $\text{Ag}_{1-x}\text{Ni}_x$  random alloy ( $0 \leq x \leq 1$ ) was thoroughly optimized using the VCA (R1) provided in the Vienna ab initio simulation package (VASP) (R2) for the *hcp* and *fcc* structures. Our DFT calculations employed the frozen-core projector augmented wave method (R3) to describe the core-valence interaction using the generalized gradient of Perdew, Burke, and Ernzerhof (R4) for the exchange-correlation functional with a cut-off energy of 450 eV for plane waves, a set of 500 k-points for the irreducible Brillouin zone, self-consistent-field convergence threshold of  $10^{-5} \text{ eV}$ , and atomic force of  $0.1 \text{ meV/\AA}$ . The electric transport properties of  $\text{Ag}_{1-x}\text{Ni}_x$  random alloy ( $0 \leq x \leq 1$ ) for the *hcp* and *fcc* structures were simulated at 400 K using the BoltzTrap code (R5) with dense k-mesh, specifically a set of 10,000 k-points for the irreducible Brillouin zone.

### 2.2. Synthesis of catalysts

The multielement random alloy based  $\text{CoNb}_2\text{O}_6 @ \text{Ag}_{0.6}\text{Ni}_{0.4}$  heterogeneous electrocatalyst was prepared using a sequential two-step process.

#### 2.2.1. Synthesis of $\text{CoNb}_2\text{O}_6$ nanocubes

Initially, highly crystalline  $\text{CoNb}_2\text{O}_6$  nanocubes were synthesized using hydrothermal methods. In a typical synthesis of  $\text{CoNb}_2\text{O}_6$  nanocubes on an fluorine-doped tin oxide FTO substrate, cobalt nitrate hexahydrate [ $\text{Co}(\text{NO}_3)_2 \cdot 6\text{H}_2\text{O}$ , 0.01 mol] and niobium ethoxide [ $\text{Nb}(\text{OCH}_2\text{CH}_3)_5$ , 0.01 mol] were mixed in 50 mL of aqueous citric acid (0.02 mol). The reaction solution was homogeneously mixed for 40 min at  $30^\circ\text{C}$  and magnetically stirred. The solution was agitated for 2 h after the addition of ethylene glycol (EG, 18 mL), polyvinyl alcohol (2.6 mmol), and hexamethylenetetramines (HMT, 0.002 mol). The resultant mixed solution was transferred to a Teflon-lined autoclave (100 mL) containing a CoNb seed layer-coated FTO plate (see the [supporting Information](#) for details on FTO cleaning and CoNb seed layer coating) and heated at  $150^\circ\text{C}$  for 15 h. The obtained sample was rinsed with deionized water and ethanol before being dried at  $30^\circ\text{C}$  for 1 h. The obtained sample was calcined in a muffle furnace at  $500^\circ\text{C}$  for 2 h to produce a cube-shaped  $\text{CoNb}_2\text{O}_6$  nanostructure.

#### 2.2.2. Synthesis of $\text{Ag}_{0.6}\text{Ni}_{0.4}$ random alloy

In accordance with standard protocol, nickel nitrate hexahydrate [ $\text{Ni}(\text{NO}_3)_2 \cdot 6\text{H}_2\text{O}$ , 8 mmol], polyvinylpyrrolidone (PVP, 20 mg), ethylene glycol (EG, 12 mmol), and hexadecyltrimethylammonium bromide (CTAB, 2 mmol) were dissolved in 50 mL citric acid (8.4 g) to form a clear solution. Then, sodium borohydride ( $\text{NaBH}_4$ , 5 mL) and silver nitrate ( $\text{Ag}(\text{NO}_3) \cdot \text{H}_2\text{O}$  18 mmol) were added to the solution, which was stirred in a round-bottom flask equipped with a reflux condenser at  $50^\circ\text{C}$  for 30 min. The reaction mixture was transferred to a Teflon-lined autoclave and heated at  $120^\circ\text{C}$  for 6 h. The as-obtained precipitate was collected and washed with ethanol and water, and the dry product was calcined at  $600^\circ\text{C}$  for 2 h in a 10%  $\text{H}_2/\text{N}_2$  flow at a heating rate of  $2^\circ\text{C}/\text{min}$  to produce an  $\text{Ag}_{0.6}\text{Ni}_{0.4}$  random alloy.  $\text{Ag}_{0.2}\text{Ni}_{0.8}$ ,  $\text{Ag}_{0.4}\text{Ni}_{0.6}$ , and  $\text{Ag}_{0.8}\text{Ni}_{0.2}$  random alloy nanoparticles were also prepared in the similar manner. For comparison, Ag and Ni metal particles were also prepared in the same way, with exclusion of  $\text{Ni}(\text{NO}_3)_2 \cdot \text{H}_2\text{O}$  or  $\text{Ag}(\text{NO}_3) \cdot \text{H}_2\text{O}$ , respectively. After heat treatment, Ni, Ag and  $\text{Ag}_{0.6}\text{Ni}_{0.4}$  samples were

used for the textural characterization and electrochemical measurement (see the details in Figs. S1 and S2 of the [Supplementary Material](#)). Elemental stoichiometric ratio of the prepared AgNi random alloy samples were examined with ICP-OES (ICP-OES, Perkin Elmer Optima 8300, see the [Table S1](#)).

### 2.2.3. Decoration of $\text{Ag}_{0.6}\text{Ni}_{0.4}$ random alloy on $\text{CoNb}_2\text{O}_6$ nanocubes

The prepared  $\text{Ag}_{0.6}\text{Ni}_{0.4}$  random alloy atoms were embedded in the  $\text{CoNb}_2\text{O}_6$  nanocubes using a simple hydrothermal method. To embed the  $\text{CoNb}_2\text{O}_6$  nanocubes, 30 mg of  $\text{Ag}_{0.6}\text{Ni}_{0.4}$  random alloy powder was dispersed into a solution comprising a mixture of 20 mL acetyl-acetone (nanoparticle-capping agent) and 5 mL  $\alpha$ -terpinol (binding agent). The resulting mixture was sonicated for 30 min at room temperature. After diluting the colloidal mixture with a 1:1 ratio of ethanol and water, it was transferred to a 100 mL Teflon-lined stainless steel autoclave containing a  $\text{CoNb}_2\text{O}_6$  nanocubes-coated FTO plate and heated at 100 °C for 1 h. The collected sample was dried and then kept at 400 °C for 1 h to obtain a final  $\text{CoNb}_2\text{O}_6$  @ $\text{Ag}_{0.6}\text{Ni}_{0.4}$  catalyst. Bulk composition of  $\text{CoNb}_2\text{O}_6$  and  $\text{CoNb}_2\text{O}_6$  @ $\text{Ag}_{0.6}\text{Ni}_{0.4}$  samples were examined with ICP-OES analysis (see the [Table S2](#)).  $\text{CoNb}_2\text{O}_6$  @ $\text{Ag}_{0.2}\text{Ni}_{0.8}$ ,  $\text{CoNb}_2\text{O}_6$  @ $\text{Ag}_{0.4}\text{Ni}_{0.6}$ , and  $\text{CoNb}_2\text{O}_6$  @ $\text{Ag}_{0.8}\text{Ni}_{0.2}$  samples were also prepared in the similar manner. For comparison,  $\text{CoNb}_2\text{O}_6$  @Ag and  $\text{CoNb}_2\text{O}_6$  @Ni catalysts were also prepared in the same way, with exclusion of  $\text{Ni}(\text{NO}_3)_2 \cdot \text{H}_2\text{O}$  or  $\text{Ag}(\text{NO}_3)_3 \cdot \text{H}_2\text{O}$ , respectively.

### 2.3. Physicochemical characterization of electrocatalysts samples

The physicochemical properties of the prepared catalyst were studied via X-ray diffraction (XRD), scanning electron microscopy (SEM), Energy-dispersive X-ray spectroscopy (EDX), high-resolution transmission electron microscopy (HR-TEM),  $\text{N}_2$  adsorption/desorption, X-ray photoelectron spectra (XPS), X-ray absorption near-edge structure (XANES), extended X-ray absorption fine structure (EXAFS), electron paramagnetic resonance (EPR), and grazing incident wide-angle X-ray scattering (GIWAX) (see [Supplementary Material](#) for detailed instrumentation and experimental protocols).

### 2.4. Electrochemical characterizations of catalysts

Linear-sweep voltammetry (LSV) and cyclic voltammetry (CV) data were collected using potentiostat/galvanostat/ZRA based on a conventional three-electrode set-up (Gamry reference 300). Electrochemical impedance spectra were conducted using an AUTOLAB/PGSTAT 128 N analyzer at a frequency range of 100 kHz–0.10 mHz in a 1 M KOH solution. The oxygen ( $\text{O}_2$ ) evolution performance was estimated in a closed cell through in situ gas chromatography (YL instrument 6500 GC system) to analyze the headspace. ORR activity of catalysts was evaluated using a rotating disk electrode (RDE, Biologic Science Instruments) connected to a Dy 2300 potentiostat in an  $\text{O}_2$ -saturated 0.1 M KOH solution (see the [Supplementary Material](#) for detailed experimental protocols).

### 2.5. Rechargeable zinc–air batteries fabrication and test

A two-electrode cell with a  $\text{CoNb}_2\text{O}_6$  @AgNi catalyst-dispersed gas diffusion layer (GDL) as the air cathode and a polished Zn plate as the anode was used to test the performance of the rechargeable Zn–air battery. Catalyst ink was spray-coated onto a GDL surface to prepare the air cathode for the Zn–air battery. In accordance with the standard technique, 10 mg catalysts, 8 mL deionized water, 2 mL isopropanol, and 0.05 mL Nafion were mixed and sonicated in an ultrasonic bath to produce a homogenous ink. Subsequently, 10  $\mu\text{L}$  of this ink was coated onto the GDL surface and dried to obtain a mass loading of  $\sim 25 \mu\text{g}/\text{cm}^2$ . The Zn–air battery performance of catalysts was examined in a 6 M KOH solution containing 0.2 M zinc acetate ( $\text{ZnC}_4\text{H}_6\text{O}_4$ ) electrolyte.

### 2.6. Measurement of rechargeable zinc–air batteries and pouch cell fabrication

The rechargeable Zn–air battery performance of the catalysts was evaluated using a two-electrode cell in a 6 M KOH solution containing a 0.2 M zinc acetate ( $\text{ZnC}_4\text{H}_6\text{O}_4$ ) electrolyte. The discharge polarization curve and peak power density of catalysts were measured using a Biologic potentiostat (Biologic, VMP-3) device. The discharge/charge cycling performance of catalysts was measured using the Wonatech cyclor system (Wonatech, WBCS3000). Additional details of the Zn–air batteries measurement and the module of Zn–air battery pouch cell fabrication have been provided in the [Supplementary Material](#).

## 3. Results and discussion

### 3.1. Calculation of electrical and electronic properties of $\text{Ag}_{1-x}\text{Ni}_x$ random alloys using VCA

A typical crystal structure of neat Ag and Ni is *hcp* and *fcc*, respectively ([Fig. 1a](#)). To understand the impact of metal composition on their crystal structure, electrical properties, and stability, we consider  $\text{Ag}_{1-x}\text{Ni}_x$  random alloy ( $0 \leq x \leq 1$ ) at the first stage using VCA (see more details in [Supplementary Material](#) and experimental section) [48,49]. Interestingly, we found that the calculated relative energy of  $\text{Ag}_{1-x}\text{Ni}_x$  random alloys are in between *hcp* and *fcc* structure and prefer to have the *hcp* structure with the lowest energy minima when approaching the portion of Ni at  $x \sim 0.4$  ([Table S3](#)). The calculated work function of  $\text{Ag}_{1-x}\text{Ni}_x$  random alloy gradually increased after adding the Ag component and approached the maximum value of  $\sim 5.4$  eV at  $x \sim 0.4$  ([Fig. 1b](#)). This indicated that the increasing portion of Ni upon Ag can promote a structural phase of transition from *fcc* to *hcp* structure with the lowest energy minima, which is in a good agreement with the earlier publications [50,51]. We anticipated that the change crystal structure of  $\text{Ag}_{1-x}\text{Ni}_x$  random alloy influences their electrical properties. In fact, the electrical conductivity  $\sigma$  of  $\text{Ag}_{1-x}\text{Ni}_x$  random alloy ( $0 \leq x \leq 1$ ) increases gradually and then increases drastically when  $x \sim 0.4$  with increasing Ag content, especially electrical conductivity  $\sigma$  of pure Ag is significantly greater than that of pure Ni ([Fig. 1c](#)).

The significant change in the electrical conductivity of  $\text{Ag}_{1-x}\text{Ni}_x$  random alloy as a function of composition ratio prompted the hypothesis that the magnetic moment of  $\text{Ag}_{1-x}\text{Ni}_x$  random alloy can be modulated. The calculated magnetic moment of  $\text{Ag}_{1-x}\text{Ni}_x$  random alloy ( $0 \leq x \leq 1$ ) for the *hcp* and *fcc* structures are provided in [Fig. 1d](#). The magnetic moment disappeared near  $x \sim 0.4$ , indicating that the electronic structure of Ni at the Fermi level should be derived from the s/p-state rather than the d-state. Hence, we evaluated the electronic structures of pure Ag, pure Ni, and  $\text{Ag}_{0.6}\text{Ni}_{0.4}$ , which revealed that the Fermi region of the pure Ni system is dominated by an incompletely filled d-state; however, the d-orbitals of pure Ag and  $\text{Ag}_{0.6}\text{Ni}_{0.4}$  are completely filled ([Fig. S3](#)). This implied that the Fermi region of pure Ag and  $\text{Ag}_{0.6}\text{Ni}_{0.4}$  are contributed from s/p states, where the effective mass  $m^*$  is substantially decreased. Therefore, it is plausible to conclude that the rapid increase in electrical conductivity ( $\sigma$ ) of  $\text{Ag}_{1-x}\text{Ni}_x$  random alloy ( $0 \leq x \leq 1$ ) at  $x \sim 0.4$  is due to the removal of magnetism associated with the electronic structure near the Fermi level, which is mostly contributed by the s/p-state rather than the d-state.

### 3.2. Multielement random alloy based $\text{CoNb}_2\text{O}_6$ @ $\text{Ag}_{0.6}\text{Ni}_{0.4}$ electrocatalysts and their structural analysis

The facile design and formation route for multielement random alloy-based  $\text{CoNb}_2\text{O}_6$  @ $\text{Ag}_{0.6}\text{Ni}_{0.4}$  heterogeneous electrocatalyst is illustrated in [Fig. 2a](#). The corresponding distinct grazing incident wide angle X-ray scattering (GIWAXS) patterns and summary of lattice parameters of the Ag, Ni,  $\text{Ag}_{0.6}\text{Ni}_{0.4}$ , and  $\text{CoNb}_2\text{O}_6$  @ $\text{Ag}_{0.6}\text{Ni}_{0.4}$  samples are shown in [Figs. S4a–4d](#) and [Table S4](#). The observed diffraction peaks of

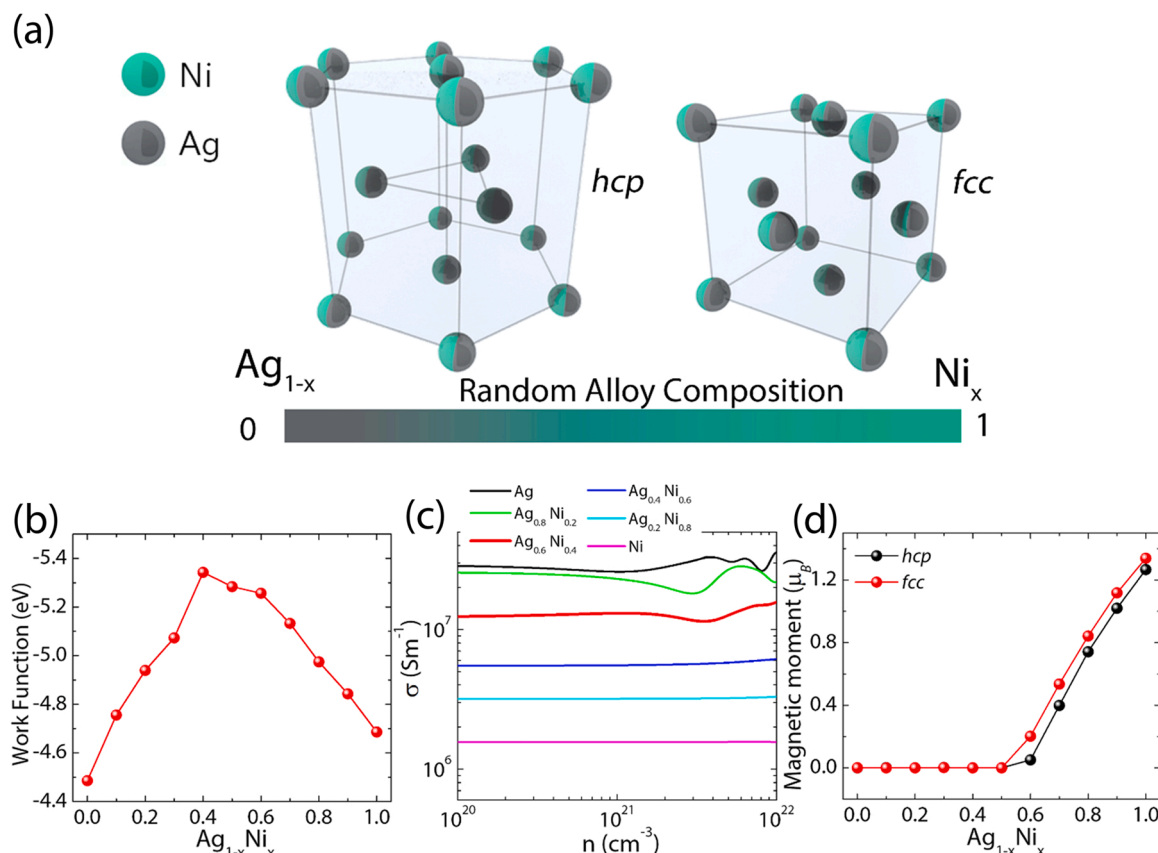


**Fig. 1.** (a) Schematic illustration of pure Ag and Ni showing a hexagonal closed-packed (*hcp*) and a face-centered cubic (*fcc*) structure, respectively. The gradient bar indicates that the AgNi random alloy can prefer to have an *hcp* structure when the portion of Ag increases. (b, c) Work function and conductivity of the  $\text{Ag}_{1-x}\text{Ni}_x$  random alloy depending on its composition ratio. (d) Magnetic moment of conductivity ( $\sigma$ ) of the  $\text{Ag}_{1-x}\text{Ni}_x$  random alloy ( $0 \leq x \leq 1$ ) for the *hcp* and *fcc* structures.

Ag metal particles for  $q$  ( $\text{\AA}^{-1}$ ) = 1.5019, 2.3787, 2.6351, and 3.0474 are indexed to the (100), (001), (120), and (200) crystal planes of the *hcp* structure, respectively. Additionally, the diffraction peaks of Ni metal for  $q$  ( $\text{\AA}^{-1}$ ) = 3.0082, 3.5939 and 4.9896 are associated with the reflection planes (111), (200), and (220), respectively, corresponding to the diffraction angles upon  $\text{Ag}_{0.6}\text{Ni}_{0.4}$  nanoparticles as compared to those of Ag and Ni metal particles. This indicated the formation of  $\text{Ag}_{0.6}\text{Ni}_{0.4}$  random alloy, conforming to hexagonal crystal structure with lattice parameters  $a = 3.3357 \text{ \AA}$ ,  $b = 3.3357 \text{ \AA}$ ,  $c = 3.4151 \text{ \AA}$ ,  $\alpha = 90^\circ$ ,  $\beta = 90^\circ$  and  $\gamma = 60^\circ$ , which is in good agreement with the results of VCA above. Moreover, a structural analysis based on the diffraction peaks of  $\text{CoNb}_2\text{O}_6$  revealed that their crystal structure correspond to an orthorhombic unit cell with lattice parameters  $a = 5.7219 \text{ \AA}$ ,  $b = 14.149 \text{ \AA}$ ,  $c = 5.0489 \text{ \AA}$ ,  $\alpha = 90^\circ$ ,  $\beta = 90^\circ$  and  $\gamma = 90^\circ$ . After  $\text{Ag}_{0.6}\text{Ni}_{0.4}$  random alloy was deposited on top of  $\text{CoNb}_2\text{O}_6$  nanostructures, the GIWAXS patterns for  $\text{CoNb}_2\text{O}_6 @ \text{Ag}_{0.6}\text{Ni}_{0.4}$  nanostructures indicated that they remained their own crystal structure. The X-ray diffraction patterns of  $\text{CoNb}_2\text{O}_6$ ,  $\text{Ag}_{0.6}\text{Ni}_{0.4}$ , and  $\text{CoNb}_2\text{O}_6 @ \text{Ag}_{0.6}\text{Ni}_{0.4}$  are displayed in Fig. S5, which corresponds to the standard PDF cards (ICDD –PDF-032–0304, JCPDS-04–0783 and JCPDS-04–0850). Interestingly, the diffraction peak of AgNi random alloy was found on the  $\text{CoNb}_2\text{O}_6 @ \text{AgNi}$  XRD result, proving that a dual-phase  $\text{CoNb}_2\text{O}_6 @ \text{AgNi}$  was successfully synthesized.

The morphological characteristics of the prepared samples were analyzed through SEM and TEM. The low- and high-magnification SEM images of  $\text{CoNb}_2\text{O}_6$  exhibit the typical hierarchical nanocube morphology (Fig. 2b, c and Fig. S6a, b). Subsequently, the atomic percentage and purity of Co, Nb, and O (14.40/27.26/58.34) were confirmed through corresponding energy dispersive X-ray spectra and

elemental mapping (Fig. S7). Fig. 2d shows the spherical-like structure of  $\text{Ag}_{0.6}\text{Ni}_{0.4}$  random alloy particles with porous nature. The EDX spectra with elemental mapping showed that the atomic percentages of Ag and Ni were 58.43% and 41.57%, respectively, which was very close to the stoichiometric ratio of  $\text{Ag}_{0.6}\text{Ni}_{0.4}$  (Fig. S8).

After the incorporation of  $\text{Ag}_{0.6}\text{Ni}_{0.4}$  random alloy nanoparticles on  $\text{CoNb}_2\text{O}_6$  nanocubes, the morphology of the  $\text{CoNb}_2\text{O}_6$  nanocubes was found to be highly preserved, as depicted by the SEM image shown in Fig. 2e. Additionally, the SEM-EDX elemental mapping of  $\text{CoNb}_2\text{O}_6 @ \text{Ag}_{0.6}\text{Ni}_{0.4}$  demonstrates that  $\text{Ag}_{0.6}\text{Ni}_{0.4}$  random alloy particles are uniformly distributed over the  $\text{CoNb}_2\text{O}_6$  nanocubes (Fig. S9). SEM images and EDX elemental mapping of  $\text{CoNb}_2\text{O}_6 @ \text{Ni}$  and  $\text{CoNb}_2\text{O}_6 @ \text{Ag}$  exhibited a similar trend to that of  $\text{CoNb}_2\text{O}_6 @ \text{Ag}_{0.6}\text{Ni}_{0.4}$ , as shown in Figs. S10, S12 and Figs. S11, S13, respectively.

To investigate the crystal structure and lattice spacing of  $\text{CoNb}_2\text{O}_6 @ \text{Ag}_{0.6}\text{Ni}_{0.4}$ , HR-TEM measurement was performed on the  $\text{Ag}_{0.6}\text{Ni}_{0.4}$  sample. The  $\text{Ag}_{0.6}\text{Ni}_{0.4}$  nanoparticles exhibited typical spherical shapes, and their lattice spacing of 0.204 and 0.236 nm was ascribed to the (111) and (111) plans (ICDD-00–004–0850, 00–004–0783) of metallic Ni and Ag of  $\text{Ag}_{0.6}\text{Ni}_{0.4}$  random alloy, respectively (Fig. 2f, g and h). The corresponding TEM-EDS mapping validated the formation of the  $\text{Ag}_{0.6}\text{Ni}_{0.4}$  random alloy shown in Fig. 2i, j and k. The low and high-magnification images of  $\text{CoNb}_2\text{O}_6$  showed a nanocube structure, which is consistent with SEM images (Fig. 3a and Figs. S14a, b). The well-resolved lattice fringe distances of 0.172 nm observed in the HR-TEM image of Fig. 3b correspond to the (062) crystal plane of  $\text{CoNb}_2\text{O}_6$  (ICDD-00–032–0304). Furthermore, the elemental mapping image of  $\text{CoNb}_2\text{O}_6$  shows that the nanocubes consist of only Co, Nb, and O (Fig. 3c). The TEM image of  $\text{CoNb}_2\text{O}_6 @ \text{Ag}_{0.6}\text{Ni}_{0.4}$  shows a homogeneous dispersion of  $\text{Ag}_{0.6}\text{Ni}_{0.4}$  random alloy on the surface of the



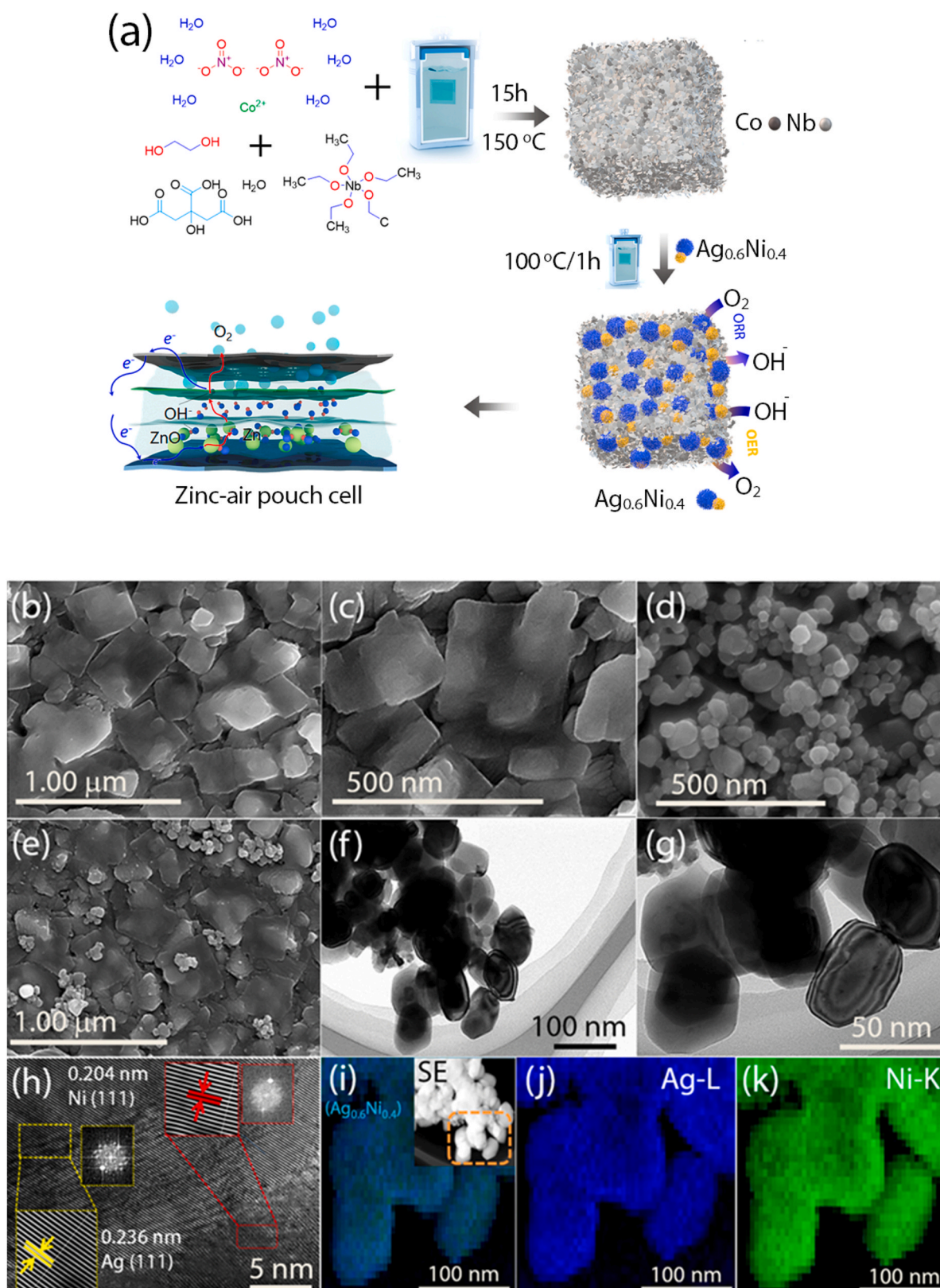


**Fig. 2.** (a) Schematic representation of the synthesis of the  $\text{Ag}_{0.6}\text{Ni}_{0.4}$  random alloy decorated with the  $\text{CoNb}_2\text{O}_6 @\text{Ag}_{0.6}\text{Ni}_{0.4}$  electrocatalyst. (b, c) Low- and high-magnification SEM images of the pristine  $\text{CoNb}_2\text{O}_6$ ; (d) SEM images of the  $\text{Ag}_{0.6}\text{Ni}_{0.4}$  random alloy particles; (e) SEM images of the  $\text{CoNb}_2\text{O}_6 @\text{Ag}_{0.6}\text{Ni}_{0.4}$ ; (f and g) low- and high-magnification HR-TEM image of the  $\text{Ag}_{0.6}\text{Ni}_{0.4}$  random alloy particles. (h) high magnification HR-TEM image, and insets corresponding lattice fringes and fast Fourier transformations (FFT) profiles of individual elements Ag and Ni taken from the respective TEM image in (h). (i, j and k) EDX mapping of AgNi and individual elements of Ag, and Ni.



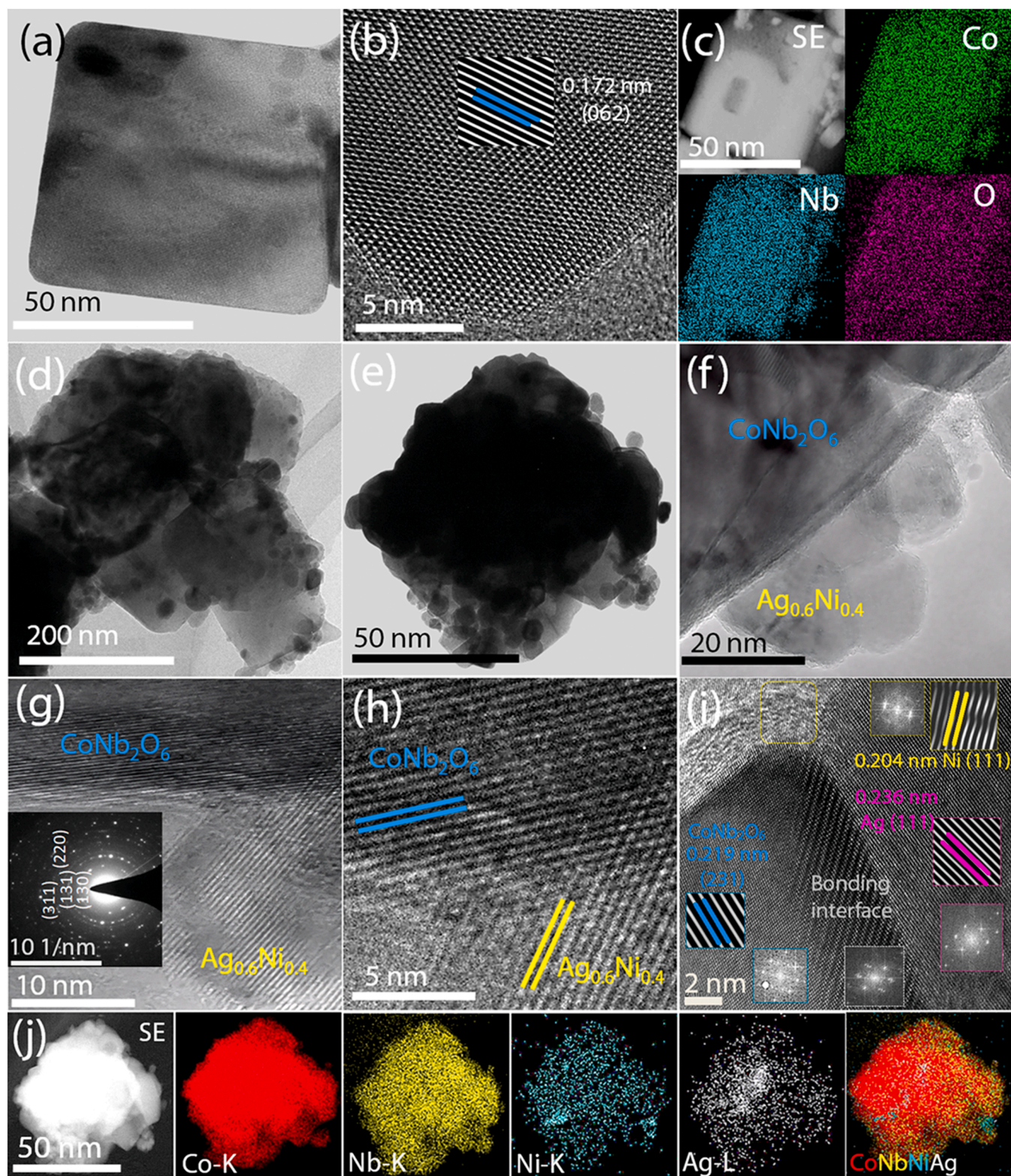


**Fig. 3.** (a) HR-TEM image of  $\text{CoNb}_2\text{O}_6$ . (b, c) High-magnification HR-TEM image, and corresponding EDS maps for individual elements of Co, Nb, and O. (d) TEM images of  $\text{CoNb}_2\text{O}_6$  @  $\text{Ag}_{0.6}\text{Ni}_{0.4}$ . (e) HR-TEM images of an individual nanocube surface anchored with  $\text{Ag}_{0.6}\text{Ni}_{0.4}$  random alloy particles. (f, g) and (h) high-magnification HR-TEM images showing the lattice fringes and (inset g) corresponding selected area electron diffraction pattern (SEAD) of  $\text{CoNb}_2\text{O}_6$  @  $\text{Ag}_{0.6}\text{Ni}_{0.4}$ . (i) Ultra-high magnification HR-TEM image, and insets corresponding lattice fringes and fast Fourier transformations (FFT) profiles of individual elements Ag, Ni,  $\text{CoNb}_2\text{O}_6$  and  $\text{CoNb}_2\text{O}_6$ - $\text{Ag}_{0.6}\text{Ni}_{0.4}$  bonding interface taken from the respective TEM image in (i). (j) STEM image and corresponding elemental maps for individual element of Co, Nb, Ni Ag and  $\text{CoNbAgNi}$ .



CoNb<sub>2</sub>O<sub>6</sub> nanocubes, maintaining the original nanocube shape without structural degradation (Fig. 3d, e and Figs. S14c–S14e). The high-resolution HR-TEM image of CoNb<sub>2</sub>O<sub>6</sub> @Ag<sub>0.6</sub>Ni<sub>0.4</sub> (Fig. 3f, g, h, i and Figs. S15) reveals a distinct interface between CoNb<sub>2</sub>O<sub>6</sub> and Ag<sub>0.6</sub>Ni<sub>0.4</sub>, confirming the coexistence of CoNb<sub>2</sub>O<sub>6</sub> and Ag<sub>0.6</sub>Ni<sub>0.4</sub> phase. The lattice spacing of 0.219 nm corresponds to the (231) crystal plane of CoNb<sub>2</sub>O<sub>6</sub> (ICDD-00–032–0304) while the observed 0.236 and 0.204 nm lattice distances relate to the metallic Ag (111) and Ni (111) crystal planes of Ag<sub>0.6</sub>Ni<sub>0.4</sub> random alloy, respectively.

Selected area electron diffraction (SAED) patterns of CoNb<sub>2</sub>O<sub>6</sub> @Ag<sub>0.6</sub>Ni<sub>0.4</sub> (Fig. 3g insets) display polycrystalline rings corresponding to the (130), (131) and (220), (311) crystal plans of CoNb<sub>2</sub>O<sub>6</sub> (ICDD-00–032–0304) and Ag<sub>0.6</sub>Ni<sub>0.4</sub> (ICDD-00–004–0850, 00–004–0783) random alloys, respectively. Additionally, EDX elemental mapping of CoNb<sub>2</sub>O<sub>6</sub> @Ag<sub>0.6</sub>Ni<sub>0.4</sub> (Fig. 3j) reveals the homogeneous dispersion of Ag<sub>0.6</sub>Ni<sub>0.4</sub> random alloy particles on the surface of CoNb<sub>2</sub>O<sub>6</sub> nanocubes, demonstrating the successful synthesis of CoNb<sub>2</sub>O<sub>6</sub> @Ag<sub>0.6</sub>Ni<sub>0.4</sub> via the proposed sequential hydrothermal method.

Through XPS, the elemental composition and surface valence state of the Ag<sub>0.6</sub>Ni<sub>0.4</sub> random alloy incorporation effect were determined. The survey XPS spectrum of the CoNb<sub>2</sub>O<sub>6</sub> @Ag<sub>0.6</sub>Ni<sub>0.4</sub> catalyst implies the existence of Co, Nb, Ag, Ni, and O elements (Fig. S16). Negative shifts were observed in the core level Co 2p and Nb 3d peaks of CoNb<sub>2</sub>O<sub>6</sub> @Ag<sub>0.6</sub>Ni<sub>0.4</sub> relative to CoNb<sub>2</sub>O<sub>6</sub> (see the details in supplementary material Figs. S17a and S17b). In contrast, the Ag 3d peaks of CoNb<sub>2</sub>O<sub>6</sub> @Ag<sub>0.6</sub>Ni<sub>0.4</sub> have higher binding energies than those of Ag<sub>0.6</sub>Ni<sub>0.4</sub> random alloy (see the details in Fig. S17c and Fig. S17d).

The peaks at 853.3 and 870.9 eV and 855.2 and 872.8 eV [52–54] in the high-resolution Ni 2p region of Ag<sub>0.6</sub>Ni<sub>0.4</sub> random alloy were attributed to spin-orbit doublets Ni<sup>0</sup> and Ni<sup>2+</sup> (Ni(OH)<sub>2</sub>), respectively (Fig. S17e). Ni<sup>0</sup> peak at 853.7 and 871.4 eV and Ni (OH)<sub>2</sub> peak at 855.5 and 873.1 eV were shifted to higher binding energies (~0.4–0.5 eV) following the integration of the Ag<sub>0.6</sub>Ni<sub>0.4</sub> random alloy on top of CoNb<sub>2</sub>O<sub>6</sub> (Fig. 4a). The intensity of Ni<sup>0</sup> peak decreased more compared to those of pristine Ag<sub>0.6</sub>Ni<sub>0.4</sub>, indicating changes in Ni oxidation states. Notably, the new peak at 854.1 eV [55,56] corresponds to NiO while the peak at 857.3 eV indicates the abundance of the Ni<sup>3+</sup> state on the surface of CoNb<sub>2</sub>O<sub>6</sub> @Ag<sub>0.6</sub>Ni<sub>0.4</sub>. Hence, it was plausible to conclude that the formation of Ni<sup>3+</sup> species can play crucial roles in oxygen electrolysis [57,58].

Three significant peaks belong to lattice oxygen (529.5 eV for M–O), hydroxyl species (531.1 eV for OH), and surface-adsorbed H<sub>2</sub>O (532.4 eV) in the O 1s spectra of CoNb<sub>2</sub>O<sub>6</sub> (Fig. 4b). However, the O 1s

spectra of CoNb<sub>2</sub>O<sub>6</sub>/Ag<sub>0.6</sub>Ni<sub>0.4</sub> shows a new peak at 530.4 eV [59,60], which should be attributed to highly oxidative oxygen species (O<sub>2</sub><sup>2−</sup>/O<sup>−</sup>) and is associated with surface oxygen vacancies [61]. The relative ratio of peak area for four oxygen species is summarized in Table S5. A relative concentration of 33.23% O<sub>2</sub><sup>2−</sup>/O<sup>−</sup> species on the CoNb<sub>2</sub>O<sub>6</sub> @Ag<sub>0.6</sub>Ni<sub>0.4</sub> surface was reported to contribute to the superior ORR and OER activities [62].

### 3.3. Electrocatalytic performance of CoNb<sub>2</sub>O<sub>6</sub> @Ag<sub>0.6</sub>Ni<sub>0.4</sub> toward the OER

To evaluate the OER electrocatalytic activity, the synthesized catalyst and commercial RuO<sub>2</sub> were used as working electrodes in a three-electrode test system containing a 1 M KOH electrolyte. As displayed in Fig. 5a, the I–R corrected LSV polarization curve of the CoNb<sub>2</sub>O<sub>6</sub> @Ag<sub>0.6</sub>Ni<sub>0.4</sub> catalyst exhibits an overpotential of 110 mV for 10 mA cm<sup>−2</sup>, which is much less than those of CoNb<sub>2</sub>O<sub>6</sub> (330 mV), CoNb<sub>2</sub>O<sub>6</sub> @Ag (250 mV), CoNb<sub>2</sub>O<sub>6</sub> @Ni (220 mV), and RuO<sub>2</sub> (300 mV), and outperforms the recently reported metal catalysts at comparable conditions (Table S6). The OER performance of CoNb<sub>2</sub>O<sub>6</sub> with different AgNi random alloy compositions is also depicted in Supplementary Material (Fig. S18, Table S7). In Particular, CoNb<sub>2</sub>O<sub>6</sub> @Ag<sub>0.6</sub>Ni<sub>0.4</sub> required a relatively low overpotential (η) of 400 mV to achieve a current density of 100 mA cm<sup>−2</sup>, compared to CoNb<sub>2</sub>O<sub>6</sub> @Ni (520 mV), CoNb<sub>2</sub>O<sub>6</sub> @Ag (620 mV), and CoNb<sub>2</sub>O<sub>6</sub> (700 mV). Accordingly, it was hypothesized that the outstanding activity of CoNb<sub>2</sub>O<sub>6</sub> @Ag<sub>0.6</sub>Ni<sub>0.4</sub> resulted from a strong electronic interaction between CoNb<sub>2</sub>O<sub>6</sub> and Ag<sub>0.6</sub>Ni<sub>0.4</sub> that modifies the local electronic structure of CoNb<sub>2</sub>O<sub>6</sub> @Ag<sub>0.6</sub>Ni<sub>0.4</sub>, and it can be confirmed that Ag<sub>0.6</sub>Ni<sub>0.4</sub> activates more reactive sites of OER. Furthermore, CoNb<sub>2</sub>O<sub>6</sub>/Ag<sub>0.6</sub>Ni<sub>0.4</sub> exhibited a small Tafel slope value of 40 mV dec<sup>−1</sup>, which is lower than CoNb<sub>2</sub>O<sub>6</sub> @Ni (50 mV dec<sup>−1</sup>), CoNb<sub>2</sub>O<sub>6</sub> @Ag (54 mV dec<sup>−1</sup>), and CoNb<sub>2</sub>O<sub>6</sub> (100 mV dec<sup>−1</sup>) counterparts and RuO<sub>2</sub> (89 mV dec<sup>−1</sup>), indicating its fast OER reaction kinetics [63–65] (Fig. 5b). Reasonably, the Tafel slope of CoNb<sub>2</sub>O<sub>6</sub> @Ag<sub>0.6</sub>Ni<sub>0.4</sub> decreases due to the introduction of the Ag<sub>0.6</sub>Ni<sub>0.4</sub> random alloy to provide a good connectivity of the CoNb<sub>2</sub>O<sub>6</sub> interface, which enhances charge and mass transfer during OER.

The excellent intrinsic activity of the CoNb<sub>2</sub>O<sub>6</sub> @Ag<sub>0.6</sub>Ni<sub>0.4</sub> catalyst is also evaluated by their larger turnover frequency (TOF) (0.2300 s<sup>−1</sup> at an overpotential of 320 mV), which is significantly higher than those of CoNb<sub>2</sub>O<sub>6</sub> @Ag (0.0118 s<sup>−1</sup>), CoNb<sub>2</sub>O<sub>6</sub> @Ni (0.0166 s<sup>−1</sup>), and CoNb<sub>2</sub>O<sub>6</sub> (0.0062 s<sup>−1</sup>) under the same overpotential condition, indicating more favorable reactive sites on the CoNb<sub>2</sub>O<sub>6</sub> @Ag<sub>0.6</sub>Ni<sub>0.4</sub> for OER reaction

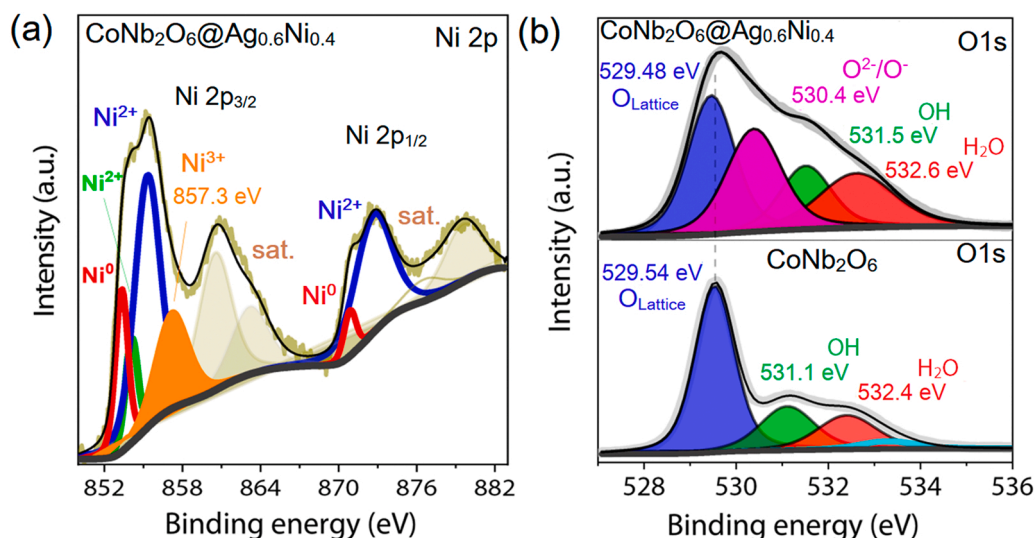
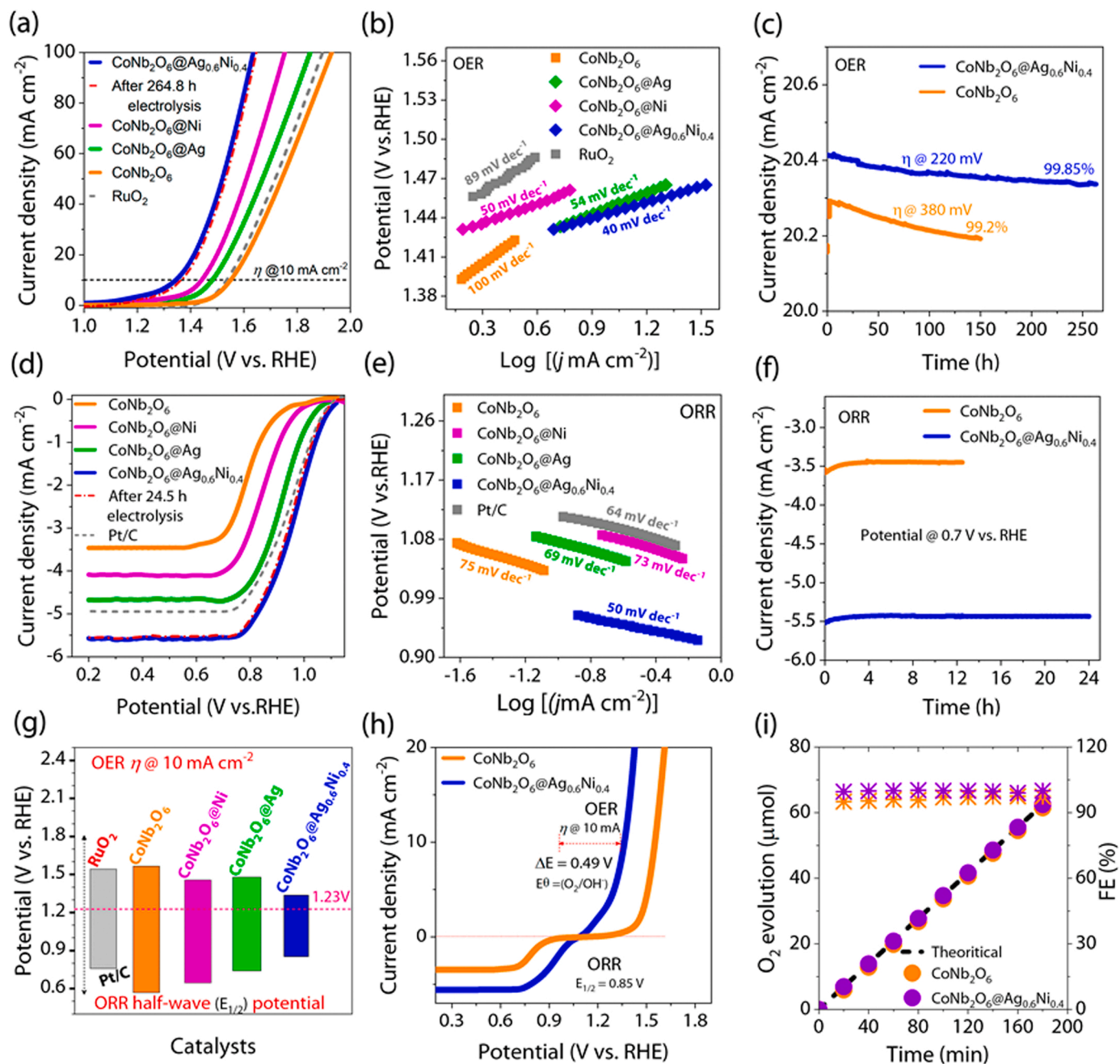


Fig. 4. (a, b) High-resolution X-ray photoelectron spectroscopy (XPS) of the Ni 2p and O 1s regions of the catalysts.



**Fig. 5.** (a) IR corrected (95%) LSV polarization curves for different catalysts at a scan rate of 5 mVs<sup>-1</sup> in 1 M KOH. The red LSV dotted line represents the after-stability testing of CoNb<sub>2</sub>O<sub>6</sub>@Ag<sub>0.6</sub>Ni<sub>0.4</sub>. (b) Corresponding Tafel plots calculated from the polarization curves. (c) Time-dependent chronoamperometric OER response of the CoNb<sub>2</sub>O<sub>6</sub> and CoNb<sub>2</sub>O<sub>6</sub>@Ag<sub>0.6</sub>Ni<sub>0.4</sub> catalysts at constant potential versus RHE. (d) ORR polarization curves recorded in an O<sub>2</sub>-saturated 0.1 M KOH at a scan rate of 5 mVs<sup>-1</sup> and rotation speed of 1600 rpm. The red ORR dotted line represents the after-stability testing of CoNb<sub>2</sub>O<sub>6</sub>@Ag<sub>0.6</sub>Ni<sub>0.4</sub>. (e) Corresponding Tafel plots and (f) time-dependent chronoamperometric ORR response of catalysts. (g) Histogram representing the comparison of OER overpotential ( $E_j = 10$ ) at a current density of 10 mAcm<sup>-2</sup> in 1 M KOH and ORR half-wave potential ( $E_{1/2}$ ) of various catalysts in 0.1 M KOH. (h) OER potential at 10 mAcm<sup>-2</sup>, ORR half-wave potential ( $E_{1/2}$ ), and their difference ( $\Delta E$ ). (i) Time-dependence of the Faradic efficiency of CoNb<sub>2</sub>O<sub>6</sub> and CoNb<sub>2</sub>O<sub>6</sub>@Ag<sub>0.6</sub>Ni<sub>0.4</sub> catalysts for theoretically and experimentally measured (from in situ gas chromatography) O<sub>2</sub> evolution at 10 mAcm<sup>-2</sup>.

(details of the calculations are provided in the [Supporting Information](#)). Moreover, to gain a better understanding of the synergistic OER activity of CoNb<sub>2</sub>O<sub>6</sub> and Ag<sub>0.6</sub>Ni<sub>0.4</sub> random alloy, the electrochemical active surface area (ECSA) of the catalysts was determined using the electrochemical double layer capacitance ( $C_{dl}$ ) derived from the CV curves in a non-Faradic potential region (Figs. S19a-S19d). As shown in Fig. S19e in the [Supporting Material](#), CoNb<sub>2</sub>O<sub>6</sub>@Ag<sub>0.6</sub>Ni<sub>0.4</sub> exhibited a larger  $C_{dl}$  of 4.89 mF cm<sup>-2</sup> than CoNb<sub>2</sub>O<sub>6</sub>@Ag (2.10 mF cm<sup>-2</sup>), CoNb<sub>2</sub>O<sub>6</sub>@Ni (2.60 mF cm<sup>-2</sup>), and CoNb<sub>2</sub>O<sub>6</sub> (1.80 mF cm<sup>-2</sup>), indicating the highest

ECSA for CoNb<sub>2</sub>O<sub>6</sub>@Ag<sub>0.6</sub>Ni<sub>0.4</sub> after incorporation of Ag<sub>0.6</sub>Ni<sub>0.4</sub> (see calculation details in the [Supporting Material](#)). Moreover, the calculated roughness factor (RF) of the catalysts has a trend similar to that of the ECSA following the order of CoNb<sub>2</sub>O<sub>6</sub>@Ag<sub>0.6</sub>Ni<sub>0.4</sub> > CoNb<sub>2</sub>O<sub>6</sub>@Ag > CoNb<sub>2</sub>O<sub>6</sub>@Ni > CoNb<sub>2</sub>O<sub>6</sub> (Table S8). CoNb<sub>2</sub>O<sub>6</sub>@Ag<sub>0.6</sub>Ni<sub>0.4</sub> with a higher RF value has been shown to have a more favorable exposed active surface for oxygen electrolysis [66].

The stability test of CoNb<sub>2</sub>O<sub>6</sub>@Ag<sub>0.6</sub>Ni<sub>0.4</sub> was performed using continuous chronoamperometric responses, which revealed that the



initial OER current density was almost maintained for 264.8 h at 220 mV, which is significantly better than the CoNb<sub>2</sub>O<sub>6</sub> @Ni (200.8 h at 280 mV), CoNb<sub>2</sub>O<sub>6</sub> @Ag (165.5 h at 330 mV) and CoNb<sub>2</sub>O<sub>6</sub> catalyst (a loss of 0.80% was observed after the continuous chronoamperometric operation of the CoNb<sub>2</sub>O<sub>6</sub> catalyst for 149 h at 380 mV (Fig. 5c, Fig. S20)). Furthermore, there is low deterioration (0.01 V) and a positive shift of the OER polarization for CoNb<sub>2</sub>O<sub>6</sub> @Ag<sub>0.6</sub>Ni<sub>0.4</sub> after 264.8 h of continuous stability testing (Fig. 4a, red dotted line), indicating the outstanding structural stability of CoNb<sub>2</sub>O<sub>6</sub> @Ag<sub>0.6</sub>Ni<sub>0.4</sub>. After performing the continuous OER activity, the structure of CoNb<sub>2</sub>O<sub>6</sub> @Ag<sub>0.6</sub>Ni<sub>0.4</sub> electrode was reexamined by the XPS, SEM and TEM under the same conditions as the initial measurement. The high resolution XPS spectra of the Co 2p, Nb 3d, and Ni 2p level spectrum in CoNb<sub>2</sub>O<sub>6</sub> @Ag<sub>0.6</sub>Ni<sub>0.4</sub> are shown in Fig. S21. The energy level XPS spectra of Co 2p and Nb 3d show slight negative peak shifts and the spectra of Ni exhibits a positive shift after the OER electrolysis. This suggests that constructing dual phase CoNb<sub>2</sub>O<sub>6</sub> @Ag<sub>0.6</sub>Ni<sub>0.4</sub> can effectively maintained the electronic structure of the Co, Nb core and optimize the adsorption of reaction intermediates, hence promoting electrocatalytic stability. SEM and TEM images of the CoNb<sub>2</sub>O<sub>6</sub> @Ag<sub>0.6</sub>Ni<sub>0.4</sub> electrode during and after a stability test are shown in Figs. S22, S23. The overall shape and structure of the catalyst was maintained and still retained original nano cube structure of CoNb<sub>2</sub>O<sub>6</sub> @Ag<sub>0.6</sub>Ni<sub>0.4</sub>, indicating the structural stability of the catalyst surface.

### 3.4. Electrocatalytic performance of CoNb<sub>2</sub>O<sub>6</sub> @Ag<sub>0.6</sub>Ni<sub>0.4</sub> toward the ORR

The corresponding ORR activity of the catalysts was evaluated using a RDE in 0.1 M KOH. LSV and cyclic voltammetry (CV) results obtained in N<sub>2</sub>-saturated and O<sub>2</sub>-saturated 0.1 M KOH for various catalysts are shown in Supplementary Material Fig. S24, S25. Polarization curves reveal that CoNb<sub>2</sub>O<sub>6</sub> @Ag<sub>0.6</sub>Ni<sub>0.4</sub> exhibits superior ORR activity compared to all other prepared catalysts (CoNb<sub>2</sub>O<sub>6</sub>, CoNb<sub>2</sub>O<sub>6</sub> @Ni, CoNb<sub>2</sub>O<sub>6</sub> @Ag, and commercial Pt/C) in terms of a more positive onset potential of 1.12 V, higher half-wave potential ( $E_{1/2}$ ) of 0.85 V, and a higher limiting current density of -5.60 mAcm<sup>-2</sup> (Fig. 5d and Table S9). Notably, the ORR activity of the CoNb<sub>2</sub>O<sub>6</sub> @Ag<sub>0.6</sub>Ni<sub>0.4</sub> catalyst outperforms the nonprecious metal catalyst reported in the literature (Table S6). Additional ORR polarization curves of CoNb<sub>2</sub>O<sub>6</sub> with various AgNi random alloy compositions are also shown in the Supplementary Material (Fig. S26, Table S7). The superior ORR performance of CoNb<sub>2</sub>O<sub>6</sub> @Ag<sub>0.6</sub>Ni<sub>0.4</sub> led us to believe that the random alloy composition of integrated CoNb<sub>2</sub>O<sub>6</sub> and Ag<sub>0.6</sub>Ni<sub>0.4</sub> can provide synergistic effects for the ORR electrolysis.

Additionally, we found that the measured Tafel slope of CoNb<sub>2</sub>O<sub>6</sub> @Ag<sub>0.6</sub>Ni<sub>0.4</sub> is 50 mVdec<sup>-1</sup>, which is less than that of CoNb<sub>2</sub>O<sub>6</sub> @Ag (69 mVdec<sup>-1</sup>), CoNb<sub>2</sub>O<sub>6</sub> @Ni (73 mVdec<sup>-1</sup>), CoNb<sub>2</sub>O<sub>6</sub> (75 mVdec<sup>-1</sup>), and Pt/C (64 mVdec<sup>-1</sup>), indicating the fast ORR kinetics on the CoNb<sub>2</sub>O<sub>6</sub> @Ag<sub>0.6</sub>Ni<sub>0.4</sub> (Fig. 5e). The electron transfer number, *n*, of the CoNb<sub>2</sub>O<sub>6</sub> and CoNb<sub>2</sub>O<sub>6</sub> @Ag<sub>0.6</sub>Ni<sub>0.4</sub> catalysts was also determined from the Koutecky-Levich (*K*-*L*) plots under various potentials (0.3–0.7 V), which were obtained from ORR polarization curves at various rotation speeds (400–1600 rpm, Figs. S27a and S27b). The *K*-*L* plots of CoNb<sub>2</sub>O<sub>6</sub> and CoNb<sub>2</sub>O<sub>6</sub> @Ag<sub>0.6</sub>Ni<sub>0.4</sub> at different potentials exhibit excellent linearity and near parallel fitting, revealing typical first-order reaction kinetics (Figs. S27c and S27d). Furthermore, the calculated electron transfer number (*n* per O<sub>2</sub>) for the CoNb<sub>2</sub>O<sub>6</sub> and CoNb<sub>2</sub>O<sub>6</sub> @Ag<sub>0.6</sub>Ni<sub>0.4</sub> catalysts was 3.9 and 4, respectively, indicating that the ORR process followed the four-electron transfer pathway closely [67]. The ORR stability of the CoNb<sub>2</sub>O<sub>6</sub>, CoNb<sub>2</sub>O<sub>6</sub> @Ag, CoNb<sub>2</sub>O<sub>6</sub> @Ni and CoNb<sub>2</sub>O<sub>6</sub> @Ag<sub>0.6</sub>Ni<sub>0.4</sub> catalysts was further evaluated through chronoamperometry testing in an O<sub>2</sub>-saturated 0.1 M KOH solution at 0.7 V (Fig. 5f, Fig. S28). The CoNb<sub>2</sub>O<sub>6</sub> @Ag<sub>0.6</sub>Ni<sub>0.4</sub> catalyst retains 98% of the initial ORR current density after 24.5 h of continuous chronoamperometric performance, indicating that the CoNb<sub>2</sub>O<sub>6</sub> @Ag<sub>0.6</sub>Ni<sub>0.4</sub> catalyst has a well

ORR-stability. In comparison to the CoNb<sub>2</sub>O<sub>6</sub> @Ag<sub>0.6</sub>Ni<sub>0.4</sub> electrocatalyst, CoNb<sub>2</sub>O<sub>6</sub> @Ag (96% after 20.1 h), CoNb<sub>2</sub>O<sub>6</sub> @Ni (96% after 18.6 h) and pristine CoNb<sub>2</sub>O<sub>6</sub> (95% after 13 h) exhibit lower stability, which further confirming that the constructed dual-phase sample of CoNb<sub>2</sub>O<sub>6</sub> @Ag<sub>0.6</sub>Ni<sub>0.4</sub> has the best ORR electrocatalytic performance. Additionally the nearly identical ORR curves before and after durability test provide further evidence of the excellent stability of CoNb<sub>2</sub>O<sub>6</sub> @Ag<sub>0.6</sub>Ni<sub>0.4</sub> (depicted using the red dotted line in Fig. 5d).

The plotted histogram compared the OER overpotential at 10 mA cm<sup>-2</sup> and the ORR half-wave potential of prepared catalysts, revealing the significantly enhanced ORR and OER performance of CoNb<sub>2</sub>O<sub>6</sub> @Ag<sub>0.6</sub>Ni<sub>0.4</sub>, which is superior to CoNb<sub>2</sub>O<sub>6</sub> and RuO<sub>2</sub> and surpasses that of Pt/C (Fig. 5g). Due to the excellent oxygen electrolysis, the overall OER and ORR activities of catalysts were further analyzed (Fig. 5h). The potential difference  $\Delta E$  ( $\Delta E = E_j = 10 - E_{1/2}$ ) between the OER potential at 10 mAcm<sup>-2</sup> and the ORR half-wave potential ( $E_{1/2}$ ) can be used to estimate the bifunctional activity of a catalyst. In general lower the  $\Delta E$  value of an electrode, the greater its bifunctionality [68]. As shown in Fig. 5h, CoNb<sub>2</sub>O<sub>6</sub> @Ag<sub>0.6</sub>Ni<sub>0.4</sub> exhibits a small  $\Delta E$  value of 0.49 V, which is smaller than those of CoNb<sub>2</sub>O<sub>6</sub> (0.99 V) and the metal-based bifunctional catalysts as reported in Tables S6.

Additionally, in situ gas chromatographic analysis was also conducted to confirm the amount of oxygen evolution. The Faradaic efficiency of CoNb<sub>2</sub>O<sub>6</sub> and CoNb<sub>2</sub>O<sub>6</sub> @Ag<sub>0.6</sub>Ni<sub>0.4</sub> catalysts at 10 mA cm<sup>-2</sup> with oxygen evolution time was measured. As shown in Fig. 5i and Fig. S29, the amount of O<sub>2</sub> volume detected with increasing operation duration is comparable to the volume calculated at constant current density, demonstrating a nearly 100% Faradaic efficiency during the OER. Furthermore, CoNb<sub>2</sub>O<sub>6</sub> @Ag<sub>0.6</sub>Ni<sub>0.4</sub> exhibited excellent methanol tolerance without any change in the ORR current when 0.5 mL (3 M) methanol was added to the O<sub>2</sub>-saturated electrolyte at 520 s (Fig. S30).

Overall, the electrocatalytic efficiency of CoNb<sub>2</sub>O<sub>6</sub> @Ag<sub>0.6</sub>Ni<sub>0.4</sub> for OER and ORR has improved significantly, likely due to the efficient charge transport and redistribution at the interface between CoNb<sub>2</sub>O<sub>6</sub> and Ag<sub>0.6</sub>Ni<sub>0.4</sub>. To gain a deeper understanding of the catalytic interaction at the CoNb<sub>2</sub>O<sub>6</sub> @Ag<sub>0.6</sub>Ni<sub>0.4</sub> interface, we conducted DFT calculations to calculate the electrical conductivity of CoNb<sub>2</sub>O<sub>6</sub> based on its charge carrier density (*n*<sub>e</sub>) and oxidation numbers (Fig. 6a). Interestingly, we found that the conductivity of CoNb<sub>2</sub>O<sub>6</sub> could be further enhanced through oxidation or reduction compared to neutral CoNb<sub>2</sub>O<sub>6</sub>, with a conductivity of approximately 3 × 10<sup>3</sup> S/m. We also observed that the conductivity of CoNb<sub>2</sub>O<sub>6</sub> gradually increased as its oxidation number increased up to +3, but decreased when its oxidation number decreased down to +3. These results can be explained by changes in the density of states (DOS). When electrons are removed from CoNb<sub>2</sub>O<sub>6</sub> (i.e., cation), the Fermi level moves closer to the broad valence band maximum (VBM), referred to as 1, which leads to a decrease in effective mass (*m*<sup>\*</sup>) and an increase in conductivity (Fig. 6b). Conversely, when electrons are added to CoNb<sub>2</sub>O<sub>6</sub> (i.e., anion), the Fermi level moves closer to the sharp conduction band maximum (CBM), referred to as 2, which leads to an increase in *m*<sup>\*</sup> and a decrease in conductivity.

Then, we compared the relative energy of CoNb<sub>2</sub>O<sub>6</sub> and Ag<sub>0.6</sub>Ni<sub>0.4</sub> using DFT calculations, considering their oxidation levels (Fig. 6c). The relative energy of CoNb<sub>2</sub>O<sub>6</sub> was found to be slightly lower than that of Ag<sub>0.6</sub>Ni<sub>0.4</sub> when an electron was removed from CoNb<sub>2</sub>O<sub>6</sub>. Conversely, the relative energy of Ag<sub>0.6</sub>Ni<sub>0.4</sub> was lower than that of CoNb<sub>2</sub>O<sub>6</sub> after an electron was added to CoNb<sub>2</sub>O<sub>6</sub>. These results imply that it is possible to secure a favorable oxidation state for efficient charge transport.

### 3.5. Chemical and electronic structure of CoNb<sub>2</sub>O<sub>6</sub> @Ag<sub>0.6</sub>Ni<sub>0.4</sub>

The local electronic properties, a coordination environment and bond distance of Ag<sub>0.6</sub>Ni<sub>0.4</sub>, CoNb<sub>2</sub>O<sub>6</sub>, and CoNb<sub>2</sub>O<sub>6</sub> @Ag<sub>0.6</sub>Ni<sub>0.4</sub> catalysts were analyzed through XANES. As shown in Fig. 7a, the normalized Co L3pre-edge XANES for CoNb<sub>2</sub>O<sub>6</sub> @Ag<sub>0.6</sub>Ni<sub>0.4</sub> showed a slightly lower energy compared to pristine CoNb<sub>2</sub>O<sub>6</sub>, indicating a shift in local

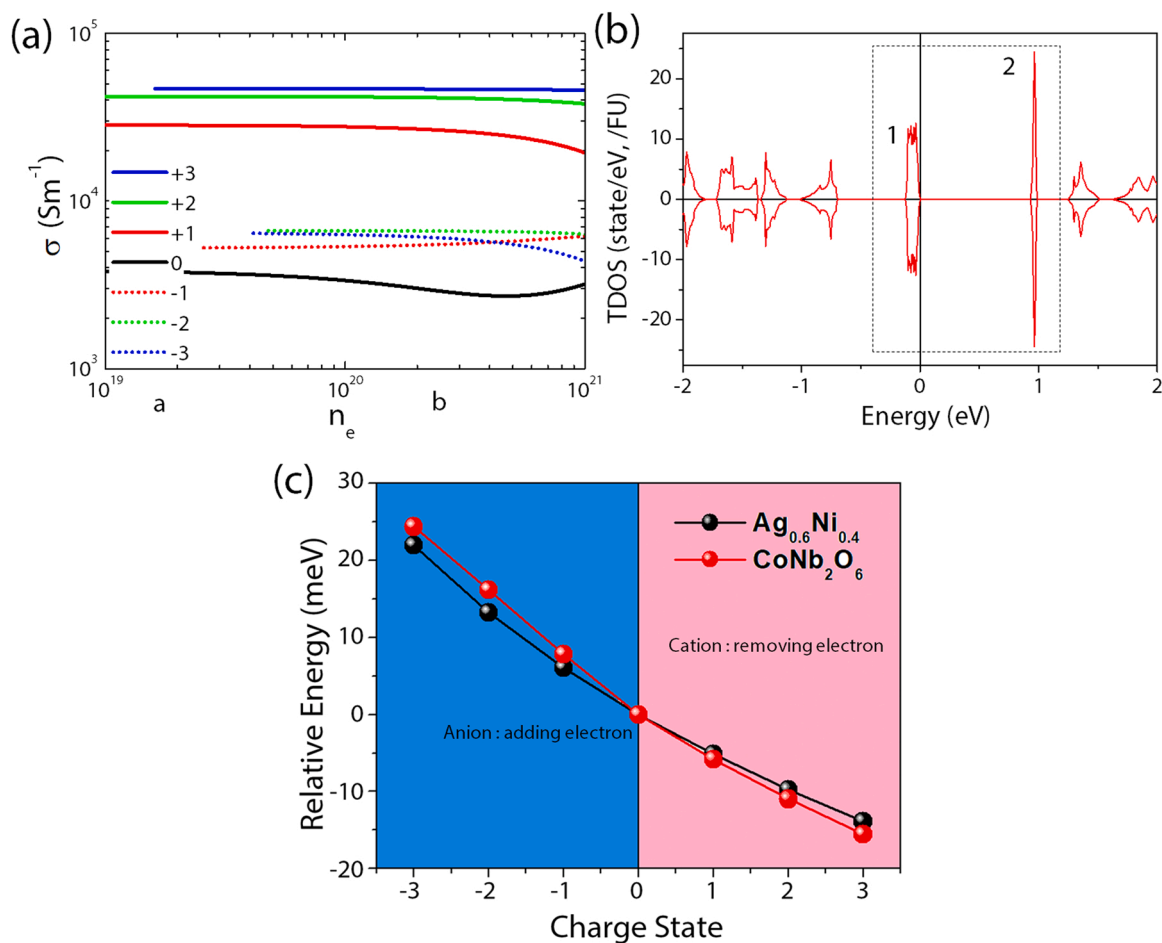


**Fig. 6.** (a) The calculated electrical conductivity of  $\text{CoNb}_2\text{O}_6$  as a change of change on  $\text{CoNb}_2\text{O}_6$ . (b) The result of calculation for density of stat (DOS) of  $\text{CoNb}_2\text{O}_6$ . 1 represents the valance band maximum (VBM) and 2 indicate the conduction band maximum (CBM) in the dash line. (c) A comparison of the relative energy change of  $\text{CoNb}_2\text{O}_6$  and  $\text{Ag}_{0.6}\text{Ni}_{0.4}$  from their neutral state when adding or removing electron.

coordination due to the presence of  $\text{Ag}_{0.6}\text{Ni}_{0.4}$  random alloy. The Ni L-edge XANES spectra for  $\text{CoNb}_2\text{O}_6 @ \text{Ag}_{0.6}\text{Ni}_{0.4}$  showed apparent changes from those of  $\text{Ag}_{0.6}\text{Ni}_{0.4}$  random alloy (Fig. 7b). The fine multiple splitting of the Ni L3 and Ni L2 peaks was attributed to the crystal field effects from the electronic structure. These characteristics, which result from the dipole transition from the 2p to the empty 3d state, were sensitive to changes in the oxidation state and local geometry of Ni [69].

Ni and Co coordination conditions in  $\text{CoNb}_2\text{O}_6 @ \text{Ag}_{0.6}\text{Ni}_{0.4}$  were further investigated using K-edge XANES spectra for Ni and Co. As shown in Fig. 7c, the shape of the pre-edge (1 s to 3d transition) and absorption edge (multiple scattering) of the normalized Ni K-edge spectra obtained from  $\text{CoNb}_2\text{O}_6 @ \text{Ag}_{0.6}\text{Ni}_{0.4}$  differs from that of the  $\text{Ag}_{0.6}\text{Ni}_{0.4}$  random alloy, indicating that there are probably local lattice strain changes around the targeted Ni atom. The Ni K-edge spectra of  $\text{CoNb}_2\text{O}_6 @ \text{Ag}_{0.6}\text{Ni}_{0.4}$  exhibited an increase in the white line and a shift of the absorption edge toward high photon energy compared to those of  $\text{Ag}_{0.6}\text{Ni}_{0.4}$  random alloy, indicating that the Ni has more empty d-orbital states and less electron density. Thus, the results matched the oxidation valence of Ni ( $\text{Ni}^{2+}$  is oxidized to  $\text{Ni}^{3+}/\text{Ni}^{4+}$ ) [70]. Comparing the Co K-edge XANES spectra (Fig. 6d) of  $\text{CoNb}_2\text{O}_6 @ \text{Ag}_{0.6}\text{Ni}_{0.4}$  to those of  $\text{CoNb}_2\text{O}_6$ , the white line is significantly reduced and the absorption edge shifts to slightly negative values, confirming the higher d-orbital occupancy due to the surface charge polarization caused by the electron transfer [71].

Fig. 6e shows the Fourier transform (FT) of EXAFS R-space Ni K-edge spectra ( $k^2$ -weighted) for  $\text{CoNb}_2\text{O}_6 @ \text{Ag}_{0.6}\text{Ni}_{0.4}$ . The dominant peak in the first coordination shell at 1.6 Å corresponds to the scattering path of

Ni–O, whereas the second coordination shell peak at 3.5 Å originated from the scattering path of Ni–Ni [72,73]. Comparatively, the decreased peak intensities of the Ni–O and Ni–Ni coordination shells are associated with lower coordination numbers and defects in the structure, reflecting changes to the electronic structure [74,75]. Besides, the FT curve of Co K-edge R-space spectrum for  $\text{CoNb}_2\text{O}_6 @ \text{Ag}_{0.6}\text{Ni}_{0.4}$  exhibits the lowest EXAFS when compared to  $\text{CoNb}_2\text{O}_6$ , demonstrating its more disordered octahedral coordination around the Co atom [76] due to the  $\text{Ag}_{0.6}\text{Ni}_{0.4}$  random alloy incorporation (Fig. S31). Additionally, the Co–O and Co–Co bond lengths of  $\text{CoNb}_2\text{O}_6 @ \text{Ag}_{0.6}\text{Ni}_{0.4}$  are 1.4 and 2.6, [77] which is shorter than those of  $\text{CoNb}_2\text{O}_6$  at 1.49 and 2.66. The contraction of Co–O and Co–Co bond length reflects the enhanced interaction between  $\text{Ag}_{0.6}\text{Ni}_{0.4}$  random alloy and  $\text{CoNb}_2\text{O}_6$ , which shifted the  $\text{CoNb}_2\text{O}_6 @ \text{Ag}_{0.6}\text{Ni}_{0.4}$  peak toward the lower energy side, as shown in Fig. S31.

As shown in Fig. 7f, the  $\text{CoNb}_2\text{O}_6$ ,  $\text{CoNb}_2\text{O}_6 @ \text{Ag}_{0.6}\text{Ni}_{0.4}$ , and  $\text{Ag}_{0.6}\text{Ni}_{0.4}$  random alloy samples exhibited significant changes near the O K-edge, indicating alterations in the local chemical and electronic structure around O atoms [78]. Notably, the main absorption edge peak below 535 eV corresponds to metal 3d band electronic transitions while the peaks at 536–543 eV relate to metal 4sp band electronic transitions [79]. Additionally, the normalized O K-edge intensity of  $\text{CoNb}_2\text{O}_6 @ \text{Ag}_{0.6}\text{Ni}_{0.4}$  is lower than that of  $\text{CoNb}_2\text{O}_6$ , and the adsorption pre-edge shifts to higher energy coupled with a new peak at 533.4 eV, indicating characteristics of oxygen vacancies [80]. From the XANES- and EXAFS data, we concluded that the incorporation of  $\text{Ag}_{0.6}\text{Ni}_{0.4}$  random alloy into  $\text{CoNb}_2\text{O}_6$  surface had been significantly affecting the Ni atoms and

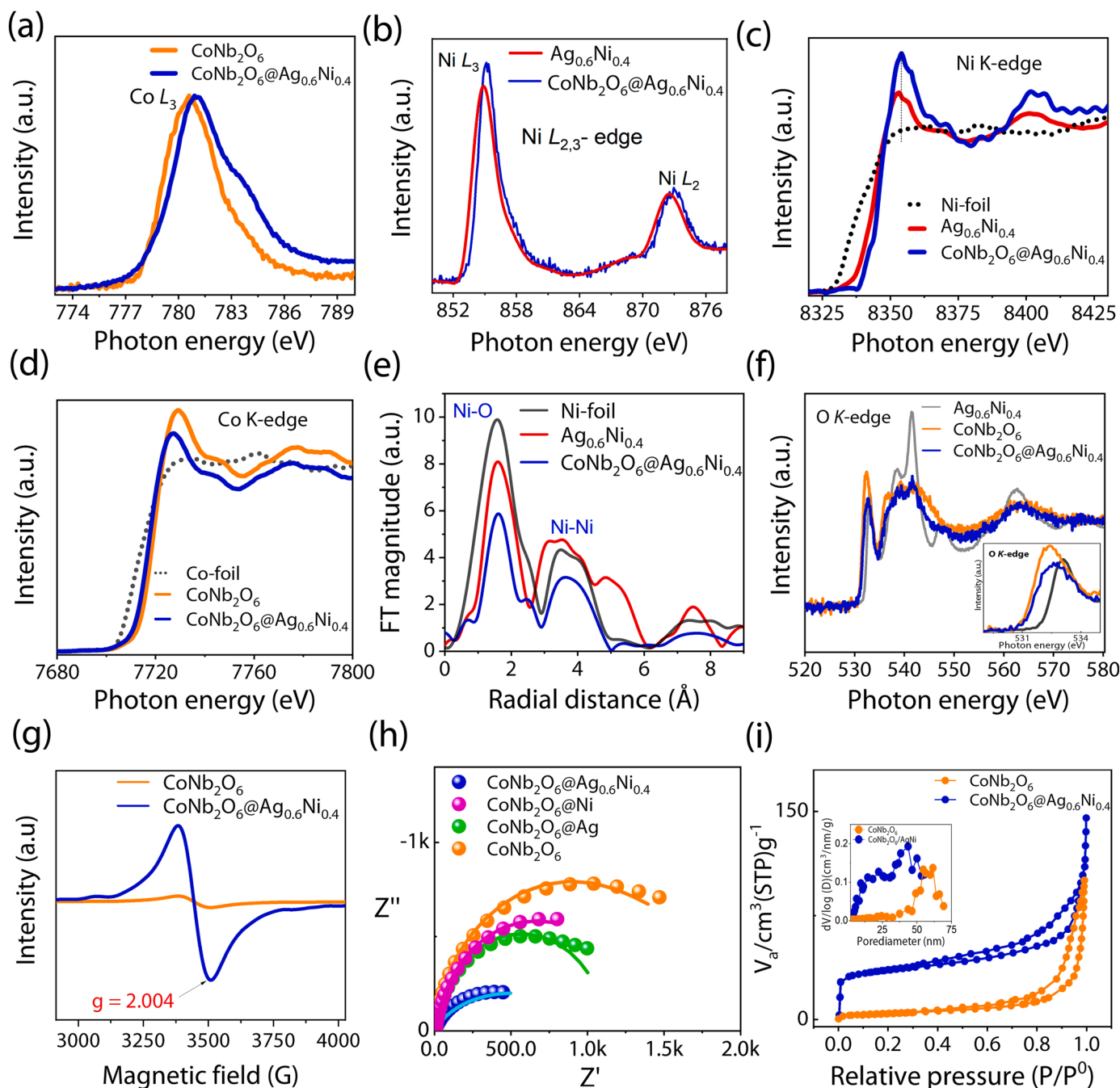


**Fig. 7.** (a) XANES spectra at the Ni L<sub>3,2</sub> edge of Ag<sub>0.6</sub>Ni<sub>0.4</sub> and CoNb<sub>2</sub>O<sub>6</sub> @Ag<sub>0.6</sub>Ni<sub>0.4</sub>. (b) Co L<sub>3,2</sub> edge XANES spectra of CoNb<sub>2</sub>O<sub>6</sub> and CoNb<sub>2</sub>O<sub>6</sub> @Ag<sub>0.6</sub>Ni<sub>0.4</sub>. (c) XANES spectra of the Ni K-edge region of Ag<sub>0.6</sub>Ni<sub>0.4</sub>, CoNb<sub>2</sub>O<sub>6</sub> @Ag<sub>0.6</sub>Ni<sub>0.4</sub>, and Ni foil. (d) XANES spectra of the Co K-edge region of the Co foil and CoNb<sub>2</sub>O<sub>6</sub> before and after Ag<sub>0.6</sub>Ni<sub>0.4</sub> incorporation. (e) Fourier transform (FT) Ni K-edge EXAFS spectra of the Ni foil, Ag<sub>0.6</sub>Ni<sub>0.4</sub>, and CoNb<sub>2</sub>O<sub>6</sub> @Ag<sub>0.6</sub>Ni<sub>0.4</sub>. (f) XANES spectra at the O K-edge of Ag<sub>0.6</sub>Ni<sub>0.4</sub>, CoNb<sub>2</sub>O<sub>6</sub>, and CoNb<sub>2</sub>O<sub>6</sub> @Ag<sub>0.6</sub>Ni<sub>0.4</sub>. (g) Electron paramagnetic spectra (EPR) of the CoNb<sub>2</sub>O<sub>6</sub> and CoNb<sub>2</sub>O<sub>6</sub> @Ag<sub>0.6</sub>Ni<sub>0.4</sub> catalysts. (h) Nyquist plots of the various catalysts fitting with equivalent circuit; the data were collected in a three-electrode configuration at 1 M KOH. (i) N<sub>2</sub> adsorption/desorption isotherms and inset corresponding pore distribution of CoNb<sub>2</sub>O<sub>6</sub> and CoNb<sub>2</sub>O<sub>6</sub> @Ag<sub>0.6</sub>Ni<sub>0.4</sub> catalysts.

oxidized to high-valence states (Ni<sup>3+</sup>), accompanying surface generate oxygen vacancies, which synergistically contribute to high ORR and OER catalytic activity of CoNb<sub>2</sub>O<sub>6</sub> @Ag<sub>0.6</sub>Ni<sub>0.4</sub>.

In addition, the K-edges of the Co and Ni of CoNb<sub>2</sub>O<sub>6</sub> @Ag<sub>0.6</sub>Ni<sub>0.4</sub> were found to shift compared to the bare CoNb<sub>2</sub>O<sub>6</sub> and Ag<sub>0.6</sub>Ni<sub>0.4</sub>. These shifts can be attributed to the formation of the interface between CoNb<sub>2</sub>O<sub>6</sub> and Ag<sub>0.6</sub>Ni<sub>0.4</sub> and promising interfacial charge transfer from Ag<sub>0.6</sub>Ni<sub>0.4</sub> to CoNb<sub>2</sub>O<sub>6</sub>. This drastically affected the local configuration of Ag<sub>0.6</sub>Ni<sub>0.4</sub> and CoNb<sub>2</sub>O<sub>6</sub> structural sites. These combined electronic and chemical properties of CoNb<sub>2</sub>O<sub>6</sub> @Ag<sub>0.6</sub>Ni<sub>0.4</sub> alter the ORR/OER

properties of the catalyst surface, generating an architecture with high conductivity and potential for active site exposure. Additionally, they offer an intuitive means of revealing bifunctional activity by monitoring the strong electronic bonding between Ag<sub>0.6</sub>Ni<sub>0.4</sub> random alloy and CoNb<sub>2</sub>O<sub>6</sub>. This allows them to maintain structural stability even when electrochemical conditions are extremely severe.

### 3.6. Oxygen vacancies, electrical and textural properties of $\text{CoNb}_2\text{O}_6$ @ $\text{Ag}_{0.6}\text{Ni}_{0.4}$

To further validate the existence of oxygen vacancies, EPR spectra of

the  $\text{CoNb}_2\text{O}_6$  @ $\text{Ag}_{0.6}\text{Ni}_{0.4}$  catalyst were acquired. As shown in Fig. 7g, the  $\text{CoNb}_2\text{O}_6$  @ $\text{Ag}_{0.6}\text{Ni}_{0.4}$  catalyst exhibits a strong EPR signal at  $g = 2.001$ , which arises from the unpaired electrons trapped in the  $\text{CoNb}_2\text{O}_6$  @ $\text{Ag}_{0.6}\text{Ni}_{0.4}$  catalyst, thus proving the existence of oxygen

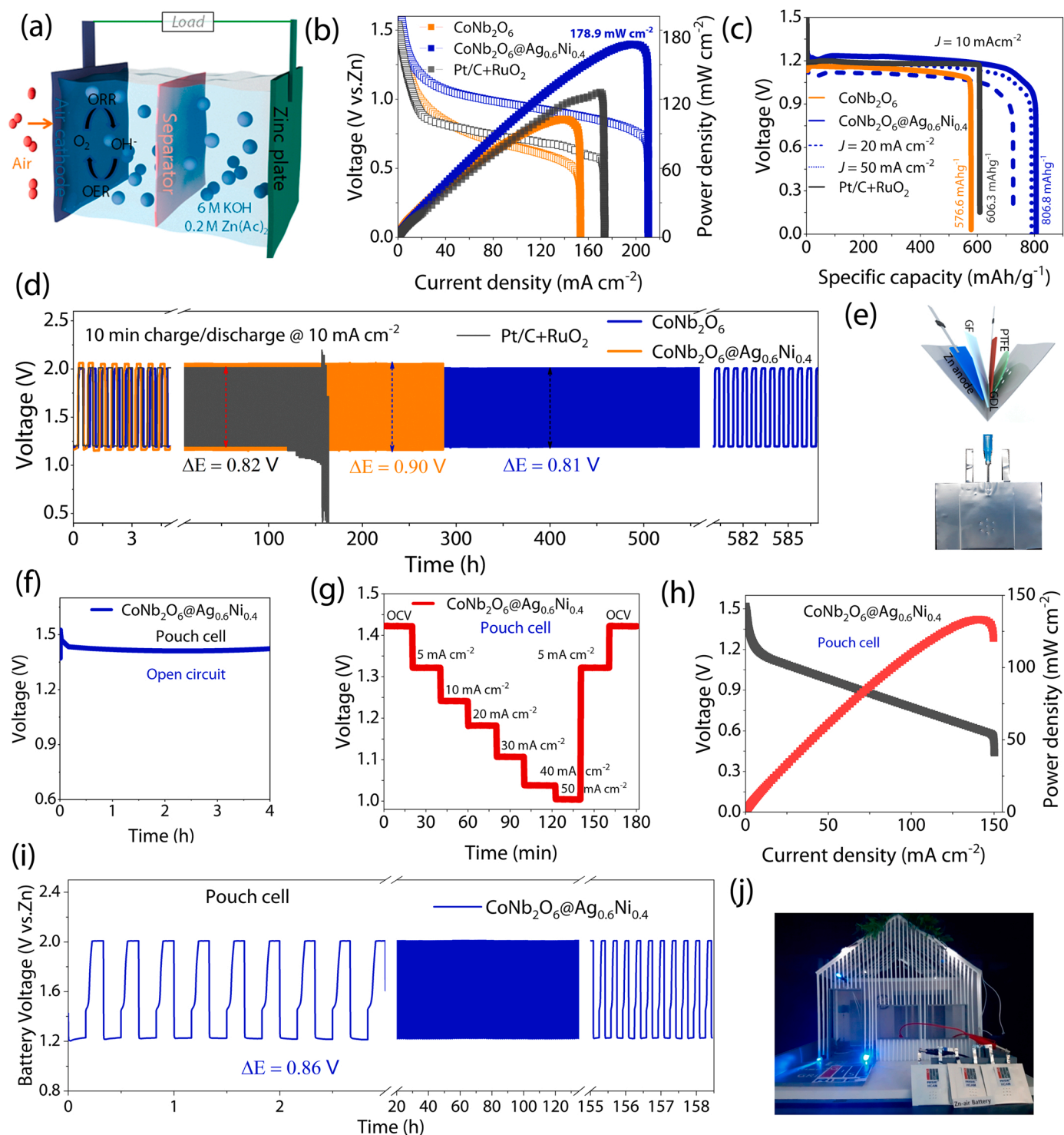


**Fig. 8.** (a) Schematic representation of the homemade Zn-air battery configuration. (b) Polarization and power density curves of Zn-air batteries based on Pt/C/RuO<sub>2</sub>,  $\text{CoNb}_2\text{O}_6$  and  $\text{CoNb}_2\text{O}_6$  @ $\text{Ag}_{0.6}\text{Ni}_{0.4}$  air cathodes. (c) Discharge specific capacities of Zn-air batteries using Pt/C/RuO<sub>2</sub>,  $\text{CoNb}_2\text{O}_6$  and  $\text{CoNb}_2\text{O}_6$  @ $\text{Ag}_{0.6}\text{Ni}_{0.4}$  air cathodes at a current density of 10  $\text{mA cm}^{-2}$  (dotted lines represent the  $\text{CoNb}_2\text{O}_6$  @ $\text{Ag}_{0.6}\text{Ni}_{0.4}$  air-cathode discharge at a current density of 20 and 50  $\text{mA cm}^{-2}$ ). (d) Discharge/charge cycling performance of Zn-air batteries with Pt/C/RuO<sub>2</sub>,  $\text{CoNb}_2\text{O}_6$  and  $\text{CoNb}_2\text{O}_6$  @ $\text{Ag}_{0.6}\text{Ni}_{0.4}$  air cathodes at a current density of 10  $\text{mA cm}^{-2}$ . (e) Schematic configuration of the Zn-air pouch cell; (f) OCP plots of Zn-air pouch cell; (g) discharge curves of  $\text{CoNb}_2\text{O}_6$  @ $\text{Ag}_{0.6}\text{Ni}_{0.4}$  catalyst driven Zn-air battery at various current densities; (h) discharge specific capacities of Zn-air batteries using pouch cell; (i) cycling performance of Zn-air pouch cells at 10  $\text{mA cm}^{-2}$ ; (j) photograph show the blue and white LED lights powered by the Zn-air pouch cell using  $\text{CoNb}_2\text{O}_6$  @ $\text{Ag}_{0.6}\text{Ni}_{0.4}$  air cathode.



vacancies induced by  $\text{Ag}_{0.6}\text{Ni}_{0.4}$  random alloy incorporation. Thus, the  $\text{CoNb}_2\text{O}_6 @ \text{Ag}_{0.6}\text{Ni}_{0.4}$  catalyst is expected to minimize the charge transfer resistance during the electrolysis. Furthermore, Fig. 7h displays the Nyquist plots derived from electrochemical impedance spectroscopy fitting for the  $\text{CoNb}_2\text{O}_6$ ,  $\text{CoNb}_2\text{O}_6 @ \text{Ag}$ ,  $\text{CoNb}_2\text{O}_6 @ \text{Ni}$ , and  $\text{CoNb}_2\text{O}_6 @ \text{Ag}_{0.6}\text{Ni}_{0.4}$  electrodes. The fitting parameters are estimated and listed in Table S10 of the supporting Information. The results revealed a substantially lower charge transfer resistance ( $R_{ct}$ ) compared to  $\text{CoNb}_2\text{O}_6$  from the fitting result, indicating that the significantly improved interfacial charge transfers can promote the reaction kinetics of the oxygen electrolysis.

Additionally, the  $\text{N}_2$  sorption isotherms (type IV isotherm with H3 hysteresis loop) of the  $\text{CoNb}_2\text{O}_6 @ \text{Ag}_{0.6}\text{Ni}_{0.4}$  catalyst indicate the existence of mesopores (Fig. 5i). Moreover, the catalyst exhibits a high Brunauer–Emmett–Teller (BET) surface area of  $198 \text{ m}^2 \text{ g}^{-1}$  compared with that of  $\text{CoNb}_2\text{O}_6$  electrode ( $93 \text{ m}^2 \text{ g}^{-1}$ ), which indicates that the  $\text{Ag}_{0.6}\text{Ni}_{0.4}$  random alloy incorporation positively enlarges the intrinsic surface area of  $\text{CoNb}_2\text{O}_6 @ \text{Ag}_{0.6}\text{Ni}_{0.4}$ . Fig. 7i inset depicts the Barrett–Joyner–Halenda pore size distribution of  $\text{CoNb}_2\text{O}_6 @ \text{Ag}_{0.6}\text{Ni}_{0.4}$  catalyst, with the majority of pores falling into a mesopores size range of 5–50 nm; these mesoporous and high specific surface area of  $\text{CoNb}_2\text{O}_6 @ \text{Ag}_{0.6}\text{Ni}_{0.4}$  significantly allow more active site, facilitating accessible mass transfer and collection efficiencies during electrolysis [81,82]. The estimated pore size, BET surface area, and pore volume of the catalysts are summarized in Table S11.

### 3.7. $\text{CoNb}_2\text{O}_6 @ \text{Ag}_{0.6}\text{Ni}_{0.4}$ as air-cathode electrocatalyst for high-performance Zinc–air battery

In addition to their excellent ORR and OER bifunctional electrocatalytic activity, rechargeable Zn–air batteries were evaluated to demonstrate the charge–discharge performance of  $\text{CoNb}_2\text{O}_6$  and  $\text{CoNb}_2\text{O}_6 @ \text{Ag}_{0.6}\text{Ni}_{0.4}$  catalysts. Fig. 8a illustrates a schematic diagram of a customized two-electrode Zn–air battery system. The Zn–air cell driven by optimized  $\text{CoNb}_2\text{O}_6 @ \text{Ag}_{0.6}\text{Ni}_{0.4}$  displays an open circuit potential (OCV) of 1.425 V (Fig. S32), which is higher than the OCV of the Zn–air cell driven by pristine  $\text{CoNb}_2\text{O}_6$  (1.41 V). This finding demonstrates the lower internal resistance of  $\text{CoNb}_2\text{O}_6 @ \text{Ag}_{0.6}\text{Ni}_{0.4}$ . The assembled zinc–air batteries polarization ( $I$ – $V$ ) curves and corresponding power density ( $P$ – $V$ ) plots are shown in Fig. 8b. Based on the discharge curve, the peak power density of the  $\text{CoNb}_2\text{O}_6 @ \text{Ag}_{0.6}\text{Ni}_{0.4}$ -air cathode battery ( $178.9 \text{ mW cm}^{-2}$  at a current density of  $213 \text{ mA cm}^{-2}$ ) is higher than that of the  $\text{Pt+C/RuO}_2$  ( $131.8 \text{ mW cm}^{-2}$  at a current density of  $173 \text{ mA cm}^{-2}$ ) and  $\text{CoNb}_2\text{O}_6$ -based Zn–air battery ( $107 \text{ mW cm}^{-2}$  at a current density of  $155 \text{ mA cm}^{-2}$ ), indicating the high catalytic activity of  $\text{CoNb}_2\text{O}_6 @ \text{Ag}_{0.6}\text{Ni}_{0.4}$  even in practical Zn–air battery conditions. The specific capacity of air cathode at various current densities is shown in Fig. 8c. At a discharge current density of  $10 \text{ mA cm}^{-2}$ , the  $\text{CoNb}_2\text{O}_6 @ \text{Ag}_{0.6}\text{Ni}_{0.4}$  air-cathode-based battery demonstrates an excellent specific capacity of  $806.8 \text{ mA h g}^{-1}$ , compared to  $606.3 \text{ mA h g}^{-1}$ ,  $576.6 \text{ mA h g}^{-1}$  of  $\text{Pt+C/RuO}_2$  and  $\text{CoNb}_2\text{O}_6$ . Furthermore, when the current density reached 20 and  $50 \text{ mA cm}^{-2}$ , the  $\text{CoNb}_2\text{O}_6 @ \text{Ag}_{0.6}\text{Ni}_{0.4}$  cathode was still capable of discharging capacities of 788.2 and  $726.4 \text{ mA h g}^{-1}$ , respectively, confirming the practical capability of the as-designed catalysts. Fig. 8d displayed the Galvanostatic discharge–charge polarization cycles for Zn–air batteries based on  $\text{CoNb}_2\text{O}_6 @ \text{Ag}_{0.6}\text{Ni}_{0.4}$ ,  $\text{RuO/PtO}$  and  $\text{CoNb}_2\text{O}_6$  air cathodes. The cycle tests were measured at room temperature at a current density of  $10 \text{ mA cm}^{-2}$ . The Zn–air batteries with  $\text{CoNb}_2\text{O}_6 @ \text{Ag}_{0.6}\text{Ni}_{0.4}$  cathodes were able to operate a long life cycle at a voltage gap of 0.81 V without voltage loss for 587 h; however, the discharge voltage of Zn–air batteries with  $\text{Pt+C/RuO}_2$  and  $\text{CoNb}_2\text{O}_6$  air cathodes decreased within 156 h and 286 h, respectively.

### 3.8. $\text{CoNb}_2\text{O}_6 @ \text{Ag}_{0.6}\text{Ni}_{0.4}$ air cathode-based rechargeable Zn–air battery pouch cell

Owing to the excellent power density, specific capacity, and cycling stability of  $\text{CoNb}_2\text{O}_6 @ \text{Ag}_{0.6}\text{Ni}_{0.4}$ , the portable Zn–air pouch cell was constructed with  $\text{CoNb}_2\text{O}_6 @ \text{Ag}_{0.6}\text{Ni}_{0.4}$  as the air cathode (see the details in Supplementary Material). Images of the  $\text{CoNb}_2\text{O}_6 @ \text{Ag}_{0.6}\text{Ni}_{0.4}$  air cathode-based rechargeable Zn–air battery pouch cell are shown in Fig. 8e and Fig. S33. The fabricated Zn–air pouch cell using  $\text{CoNb}_2\text{O}_6 @ \text{Ag}_{0.6}\text{Ni}_{0.4}$  catalyst as the air cathode (Fig. 8f) demonstrates an OCV of 1.41 V and a specific capacity of  $716.6 \text{ mA h g}^{-1}$  (at  $30 \text{ mA cm}^{-2}$  (Fig. S34)) based on the mass of consumed Zn (93.4% of the theoretical capacity). The galvanostatic discharge measurements (Fig. 8g) of the  $\text{CoNb}_2\text{O}_6 @ \text{Ag}_{0.6}\text{Ni}_{0.4}$ -catalyzed Zn–air pouch cell show a small voltage drop between 5 and  $50 \text{ mA cm}^{-2}$ . Additionally, when the current density is lowered to  $10 \text{ mA cm}^{-2}$ , the discharge can be reversed, demonstrating that the discharge voltage rate performance and their reversibility are excellent. The peak power density of the pouch cell was measured to be  $135.6 \text{ mW cm}^{-2}$  at  $150 \text{ mA cm}^{-2}$  (Fig. 8h). As shown in Fig. 8i, the cycling stability of a  $\text{CoNb}_2\text{O}_6 @ \text{Ag}_{0.6}\text{Ni}_{0.4}$  air-cathode-based battery was studied at a current density of  $10 \text{ mA cm}^{-2}$  and a charging and discharging duration of 10 min each. The Zn–air pouch cell with  $\text{CoNb}_2\text{O}_6 @ \text{Ag}_{0.6}\text{Ni}_{0.4}$  air cathode has a small charge–discharge voltage gap of 0.86 V. After 158.6 h of cycling,  $\text{CoNb}_2\text{O}_6 @ \text{Ag}_{0.6}\text{Ni}_{0.4}$ -based batteries exhibited a minor voltage drop of 0.03 V, demonstrating their excellent stability. Following cycling performance, three fabricated pouch cells integrated in series with ultrasonic welding (OCV is 4.23 V, a single battery is 1.41 V) lit an LED house for several hours (Fig. 8j), demonstrating the application potential of the prepared  $\text{CoNb}_2\text{O}_6 @ \text{Ag}_{0.6}\text{Ni}_{0.4}$  air cathode.

## 4. Conclusions

In conclusion, we provided an efficient sequential hydrothermal method for the fabrication of highly dispersive mesoporous  $\text{Ag}_{0.6}\text{Ni}_{0.4}$  random alloy nanoparticles on  $\text{CoNb}_2\text{O}_6$  nanocubes. The random alloy based  $\text{CoNb}_2\text{O}_6 @ \text{Ag}_{0.6}\text{Ni}_{0.4}$  heterogeneous catalyst demonstrated outstanding ORR and OER activities and remarkable stability in alkaline environments. Detailed simulation and characterization data, including VCA, XPS, XNEAS, XRFA, and advanced electrochemical experiments, revealed that the improved electrochemical performance of the  $\text{CoNb}_2\text{O}_6 @ \text{Ag}_{0.6}\text{Ni}_{0.4}$  catalyst is likely attributable to the incorporation of  $\text{Ag}_{0.6}\text{Ni}_{0.4}$  random alloy. This modified the electrical and chemical properties of  $\text{CoNb}_2\text{O}_6$  and created  $\text{CoNb}_2\text{O}_6 @ \text{Ag}_{0.6}\text{Ni}_{0.4}$  with high conductivity and the possibility for active site exposure. The formation of defect-enriched surface,  $\text{Ni}^{3+}$  active intermediates, an abundance of highly oxidative oxygen species, and a mesoporous structure resulted in additional catalytic support, which improved overall electrochemical performance. The strong electronic bonding and structural advantages of  $\text{CoNb}_2\text{O}_6 @ \text{Ag}_{0.6}\text{Ni}_{0.4}$  facilitated charge transfer and ensured structural stability even under extreme electrochemical conditions. The  $\text{CoNb}_2\text{O}_6 @ \text{Ag}_{0.6}\text{Ni}_{0.4}$  air cathode delivered excellent specific capacity ( $806.8 \text{ mA h g}^{-1}$  at  $10 \text{ mA cm}^{-2}$ ), power densities ( $178.9 \text{ mW cm}^{-2}$  at  $213 \text{ mA cm}^{-2}$ ), and stable cycling life in Zn–air battery applications ( $587 \text{ h}$  at  $10 \text{ mA cm}^{-2}$ ). Exceptionally, the designed pouch-type zinc–air batteries possessed a peak power density of  $135.6 \text{ mW cm}^{-2}$  at  $150 \text{ mA cm}^{-2}$ , excellent rate capability, and a stable discharge/charge cycle life of over 158.6 h at  $10 \text{ mA cm}^{-2}$ . The proposed fabrication of random alloy dispersed  $\text{CoNb}_2\text{O}_6 @ \text{Ag}_{0.6}\text{Ni}_{0.4}$  catalysts facilitated the construction of various metal alloy catalyst systems for numerous sustainable energy conversion technologies.

### CRedit authorship contribution statement

**Chandran Balamurugan:** Project conception and organization, Investigation, Sample and device fabrication, Formal analysis,

Interpretation of data, Visualization, Writing - original draft, Writing-review. **Changhoon Lee**: DFT calculation & Interpretation, Visualization. **Kyusang Cho**: Helped in device fabrication & characterization, Validation. **Jehan Kim**: GIWAXS measurements & Validation. **Byoungwook Park**: Graphical support. **Woochul Kim**: Helped in materials characterization. **Namsu Lim**: Helped in materials characterization. **Hyeonhuh Kim**: Helped in materials characterization. **Yusin Pak**: Equipment provision and discussions. **Keun Hwa Chae**: Materials characterization, Validation. **Ji Hoon Shim**: Equipment provision and discussions. **Sooncheol Kwon**: Project conception and organization, supervision, Interpretation of data, Writing & editing of manuscript.

## Declaration of Competing Interest

The authors declare that they have no known competing financial interests or personal relationships that could have appeared to influence the work reported in this paper.

## Data Availability

Data will be made available on request.

## Acknowledgements

This research was supported by the Young Researchers Program of the NRF funded by the Ministry of Science, ICT & Future Planning (NRF-2021R1A2C4001904). This research was supported by Basic Science Research Program through the National Research Foundation of Korea (NRF) funded by the Ministry of Education (NRF-2022R1I1A1A01072238). This work was supported by the National Research Foundation of Korea (NRF) funded by the Ministry of Science and ICT (NRF-2022M3H4A1A04074153; NRF-2020M3H4A2084417; NRF-2022M3C1A3091988). This research at MPK/POSTECH was supported by Basic Science Research Program through the National Research Foundation of Korea (NRF) funded by the Ministry of Education (NRF-2021R1F1A1063478).

## Appendix A. Supporting information

Supplementary data associated with this article can be found in the online version at doi:10.1016/j.apcatb.2023.122631.

## References

- [1] Z.W. Seh, J. Kibsgaard, C.F. Dickens, I. Chorkendorff, J.K. Nørskov, T.F. Jaramillo, Combining theory and experiment in electrocatalysis: Insights into materials design, *Science* 355 (2017) 4998.
- [2] M. Armand, J.M. Tarascon, Building better batteries, *Nature* 451 (2008) 652–657.
- [3] P.G. Bruce, S.A. Freunberger, L.J. Hardwick, J.-M. Tarascon, Tarascon, Li–O<sub>2</sub> and Li–S batteries with high energy storage, *Nat. Mater.* 11 (2012) 19–29.
- [4] Y. Du, B. Li, G. Xu, L. Wang, Recent advances in interface engineering strategy for highly-efficient electrocatalytic water splitting, *InfoMat* 5 (2023), e12377.
- [5] Z. Yang, J. Zhang, M.C.W. K-Meyer, X. Lu, D. Choi, J.P. Lemmon, J. Liu, Electrochemical Energy Storage for Green Grid, *Chem. Rev.* 111 (2011) 3577–3613.
- [6] D. Frattini, E.G. Gaitan, A.B. Murguialday, M. Armand, N.O. Vitoriano, Essential data for industrially relevant development of bifunctional cathodes and biopolymer electrolytes in solid-state zinc–air secondary batteries, *Energy Environ. Sci.* 15 (2022) 5039–5058.
- [7] S. Lei, Z. Liu, C. Liu, J. Li, B. Lu, S. Liang, J. Zhou, Opportunities for biocompatible and safe zinc-based batteries, *Energy Environ. Sci.* 15 (2022) 4911–4927.
- [8] J.-S. Lee, S.T. Kim, R. Cao, N.-S. Choi, M. Liu, K.T. Lee, J. Cho, Metal–air batteries with high energy density: Li–air versus Zn–air, *Adv. Energy Mater.* 1 (2011) 34–50.
- [9] Y. Xu, Y. Zhang, Z. Guo, J. Ren, Y. Wang, H. Peng, Flexible, stretchable, and rechargeable fiber-shaped zinc–air battery based on cross-stacked carbon nanotube sheets, *Angew. Chem.* 54 (2015) 15390–15394.
- [10] J. Fu, Z.P. Cano, M.G. Park, A. Yu, M. Fowler, Z. Chen, Electrically rechargeable zinc–air batteries: progress, challenges, and perspectives, *Adv. Mater.* 29 (2017), 1604685.
- [11] J. Pan, Y.Y. Xu, H. Yang, Z. Dong, H. Liu, B.Y. Xia, Advanced architectures and relatives of air electrodes in Zn–air batteries, *Adv. Sci.* 5 (2018), 1700691.
- [12] L. Ma, S. Chen, Z. Pei, H. Li, Z. Wang, Z. Liu, Z. Tang, J.A. Zapien, C. Zhi, Flexible waterproof rechargeable hybrid zinc batteries initiated by multifunctional oxygen vacancies-rich cobalt oxide, *ACS Nano* 12 (2018) 8597–8605.
- [13] W. Liu, B. Ren, W. Zhang, M. Zhang, G. Li, M. Xiao, J. Zhu, A. Yu, L. R-Sandoval, Z. Chen, Defect-enriched nitrogen doped–graphene quantum dots engineered NiCo<sub>2</sub>S<sub>4</sub> nanoarray as high-efficiency bifunctional catalyst for flexible Zn–air battery, *Small* 15 (2019), 1903610.
- [14] W. Liu, J. Feng, T. Wei, Q. Liu, S. Zhang, Y. Luo, J. Luo, X. Liu, Active-site and interface engineering of cathode materials for aqueous Zn–gas batteries, *Nano Res* 16 (2023) 2325–2346.
- [15] Q. Lu, X. Zou, K. Liao, R. Ran, W. Zhou, M. Ni, Z. Shao, Direct growth of ordered N-doped carbon nanotube arrays on carbon fiber cloth as a free-standing and binder-free air electrode for flexible quasi-solid-state rechargeable Zn–Air batteries, *Carbon Energy* 2 (2020) 461–471.
- [16] J. Park, M. Risch, G. Nam, M. Park, T.J. Shin, S. Park, M.G. Kim, Y.S. Horn, J. Cho, Single crystalline pyrochlore nanoparticles with metallic conduction as efficient bifunctional oxygen electrocatalysts for Zn–air batteries, *Energy Environ. Sci.* 10 (2017) 129–136.
- [17] H.-F. Wang, Q. Xu, Materials design for rechargeable metal–air batteries, *Mater* 4 (2019) 565–595.
- [18] J. Fu, R. Liang, G. Liu, A. Yu, Z. Bai, L. Yang, Z. Chen, Recent progress in electrically rechargeable zinc–air batteries, *Adv. Mater.* 31 (2018), 1805230.
- [19] R. Cao, J.-S. Lee, M. Liu, J. Cho, Recent progress in non-precious catalysts for metal–air batteries, *Adv. Energy Mater.* 2 (2012) 816–829.
- [20] J.-S. Lee, T. Lee, H.-K. Song, J. Cho, B.-S. Kim, Ionic liquid modified graphene nanosheets anchoring manganese oxide nano-particles as efficient electrocatalysts for Zn–air batteries, *Energy Environ. Sci.* 4 (2011) 4148–4154.
- [21] C. Lai, J. Fang, X. Liu, M. Gong, T. Zhao, T. Shen, K. Wang, K. Jiang, D. Wang, In situ coupling of NiFe nanoparticles with N-doped carbon nanofibers for Zn–air batteries driven water splitting, *Appl. Catal. B-Environ.* 285 (2021), 119856.
- [22] D. Wang, Y.-P. Deng, Y. Zhang, Y. Zhao, G. Zhou, L. Shui, Y. Hud, M. Shakouri, X. Wang, Z. Chen, Defect engineering on three-dimensionally ordered macroporous phosphorus doped Co<sub>3</sub>O<sub>4-δ</sub> microspheres as an efficient bifunctional electrocatalyst for Zn–air batteries, *Energy Storage Mater.* 41 (2021) 427–435.
- [23] Y. Li, Y. Sun, Y. Qin, W. Zhang, L. Wang, M. Luo, H. Yang, S. Guo, Recent advances on water–splitting electrocatalysis mediated by noble–metal–based nanostructured materials, *Adv. Energy Mater.* 10 (2020), 1903120.
- [24] J. Liu, C. Wang, H. Sun, H. Wang, F. Rong, L. He, Y. Lou, S. Zhang, Z. Zhang, M. Du, CoO<sub>x</sub>/CoN<sub>y</sub> nanoparticles encapsulated carbon-nitride nanosheets as an efficiently trifunctional electrocatalyst for overall water splitting and Zn–air battery, *Appl. Catal. B-Environ.* 279 (2020), 119407.
- [25] Y. Du, H. Sheng, D. Astruc, M. Zhu, Atomically precise noble metal nanoclusters as efficient catalysts: a bridge between structure and properties, *Chem. Rev.* 120 (2020) 526–622.
- [26] J. Balamurugan, T.T. Nguyen, D.H. Kim, N.H. Kim, J.H. Lee, 3D nickel molybdenum oxyselenide (Ni<sub>1-x</sub>Mo<sub>x</sub>OSe) nanoarchitectures as advanced multifunctional catalyst for Zn–air batteries and water splitting, *Appl. Catal. B-Environ.* 286 (2021), 119909.
- [27] S. Dou, L. Tao, J. Huo, S. Wang, L. Dai, Etched and doped Co<sub>9</sub>S<sub>8</sub>/graphene hybrid for oxygen electrocatalysis, *Energy Environ. Sci.* 9 (2016) 1320–1326.
- [28] H. Osgood, S.V. Devaguptapu, H. Xu, J. Cho, G. Wu, Transition metal (Fe, Co, Ni, and Mn) oxides for oxygen reduction and evolution bifunctional catalysts in alkaline media, *Nano Today* 11 (2016) 601–625.
- [29] X. Han, W. Zhang, X. Ma, C. Zhong, N. Zhao, W. Hu, Y. Deng, Identifying the activation of bimetallic sites in NiCo<sub>2</sub>S<sub>4</sub>@g-C<sub>3</sub>N<sub>4</sub>-CNT hybrid electrocatalysts for synergistic oxygen reduction and evolution, *Adv. Mater.* 31 (2019), 1808281.
- [30] W. Liu, J. Zhang, Z. Bai, G. Jiang, M. Li, K. Feng, L. Yang, Y. Ding, T. Yu, Z. Chen, A. Yu, Controllable urchin-like NiCo<sub>2</sub>S<sub>4</sub> microsphere synergized with sulfur-doped graphene as bifunctional catalyst for superior rechargeable Zn–Air battery, *Adv. Funct. Mater.* 28 (2018), 1706675.
- [31] M. Yang, Y. Liu, J. Sun, S. Zhang, X. Liu, J. Luo, Integration of partially phosphatized bimetal centers into trifunctional catalyst for high-performance hydrogen production and flexible Zn–air battery, *Sci. China Mater.* 65 (2022) 1176–1186.
- [32] Y. Wang, N. Xu, R. He, L. Peng, D. Cai, J. Qiao, Large-scale defect-engineering tailored tri-doped graphene as a metal-free bifunctional catalyst for superior electrocatalytic oxygen reaction in rechargeable Zn–air battery, *Appl. Catal. B-Environ.* 285 (2021), 119811.
- [33] X. Han, X. Wu, C. Zhong, Y. Deng, N. Zhao, W. Hu, NiCo<sub>2</sub>S<sub>4</sub> nanocrystals anchored on nitrogen-doped carbon nanotubes as a highly efficient bifunctional electrocatalyst for rechargeable zinc–air batteries, *Nano Energy* 31 (2017) 541–550.
- [34] H. Liu, X. Ma, Y. Rao, Y. Liu, J. Liu, L. Wang, M. Wu, Heteromorphic NiCo<sub>2</sub>S<sub>4</sub>/Ni<sub>3</sub>S<sub>2</sub>/Ni foam as a self-standing electrode for hydrogen evolution reaction in alkaline solution, *ACS Appl. Mater. Interfaces* 10 (2018) 10890–10897.
- [35] Z. Zhang, Y.-P. Deng, Z. Xing, D. Luo, S. Sy, Z.P. Cano, G. Liu, Y. Jiang, Z. Chen, “Ship in a bottle” design of highly efficient bifunctional electrocatalysts for long-lasting rechargeable Zn–air batteries, *ACS Nano* 13 (2019) 7062–7072.
- [36] J. Li, Y. Zhu, W. Chen, Z. Lu, J. Xu, A. Pei, Y. Peng, X. Zheng, Z. Zhang, S. Chu, Y. Cui, Breathing-mimicking electrocatalysis for oxygen evolution and reduction, *Joule* 3 (2019) 557–569.
- [37] G. Nam, J. Park, M. Choi, P. Oh, S. Park, M.G. Kim, N. Park, J. Cho, J.-S. Lee, Carbon-coated core–shell Fe–Cu nanoparticles as highly active and durable electrocatalysts for a Zn–air battery, *ACS nano* 9 (2015) 6493–6501.

- [38] J.R. McKone, B.F. Sadler, C.A. Werlang, N.S. Lewis, H.B. Gray, Ni–Mo nanopowders for efficient electrochemical hydrogen evolution, *ACS Catal.* 3 (2013) 166–169.
- [39] X. Fu, J. Zhang, S. Zhan, F. Xi, C. Wang, D. Ma, Q. Yue, J. Wud, Y. Kang, High-entropy alloy nanosheets for fine-tuning hydrogen evolution, *ACS Catal.* 12 (2022) 11955–11959.
- [40] Yu Ding, Bo-Qiang Miao, Ya-Chong Liu, Nan Hou, Yun Yang, Pu-Jun Jin, Shi-Bin Yin, Yu Chen, Rhodium-cobalt alloy nanotubes toward methanol oxidation reaction, *Small Struct.* 3 (2022), 2200046.
- [41] D. Cao, H. Xu, D. Cheng, Construction of defect-rich RhCu nanotubes with highly active Rh<sub>3</sub>Cu<sub>1</sub> alloy phase for overall water splitting in all pH values, *Adv. Energy Mater.* 10 (2020), 1903038.
- [42] A. Yu, S.Y. Kim, C. Lee, M.H. Kim, Y. Lee, Boosted electron-transfer kinetics of hydrogen evolution reaction at bimetallic RhCo alloy nanotubes in acidic solution, *ACS Appl. Mater. Interfaces* 11 (2019) 46886–46893.
- [43] S. Gao, T. Wang, M. Jin, S. Zhang, Q. Liu, G. Hu, Hui Yang, Jun Luo, Xijun Liu, Bifunctional Nb–N–C atomic catalyst for aqueous Zn–air battery driving CO<sub>2</sub> electrolysis, *China Mater.* (2022), <https://doi.org/10.1007/s40843-022-2236-8>.
- [44] J.-Y. Zhang, T. He, M. Wang, R. Qi, Y. Yan, Z. Dong, H. Liu, H. Wang, B. YuX, Energy-saving hydrogen production coupling urea oxidation over a bifunctional nickel–molybdenum nanotube array, *Nano Energy* 60 (2019) 894–902.
- [45] R. Majee, A. Kumar, T. Das, S. Chakraborty, S. Bhattacharyya, Tweaking nickel with minimal silver in a heterogeneous alloy of decahedral geometry to deliver platinum-like hydrogen evolution activity, *Angew. Chem.* 59 (2020) 2881–2889.
- [46] C. Balamurugan, C. Lee, K. Cho, J. Kim, B. Park, Y. Pak, J. Kong, S. Kwon, Hydrothermally grown dual-phase heterogeneous electrocatalysts for highly efficient rechargeable metal–air batteries with long-term stability, *Adv. Sci.* 9 (2022), 2203663.
- [47] C. Wang, H. Lu, Z. Mao, C. Yan, G. Shen, X. Wang, Bimetal Schottky Heterojunction Boosting Energy-Saving Hydrogen Production from Alkaline Water via Urea Electrocatalysis, *Adv. Funct. Mater.* 30 (2020), 2000556.
- [48] M.I. Novgorodova, A.I. Gorshkov, A.V. Mokhov, Native silver and its new structural modifications, *Int. Geol. Rev.* 23 (1981) 485–494.
- [49] M. Yousuf, P.C. Sahu, H.K. Jajoo, S. Rajagopalan, K. Govinda Rajan, Effect of magnetic transition on the lattice expansion of nickel, *J. Phys. F.* 16 (1986) 373–380.
- [50] T. Jin, H.S. Ji, Y.J. Lee, J.Y. Kim, S.K. Kwon, C. Lee, J.H. Shim, Descriptor-based crystal structure prediction of magnetic transition metals: Orbital-spin occupancy rule, *AIP Adv.* 8 (2018), 065020.
- [51] T. Jin, I. Park, T. Park, J. Park, J.H. Shim, Accelerated crystal structure prediction of multi-elements random alloy using expandable features, *Sci. Rep.* 11 (2021) 5194.
- [52] C. Balamurugan, S. Song, H. Jo, J. Seo, GdFeO<sub>3</sub> Perovskite oxide decorated by group X heterometal oxides and bifunctional oxygen electrocatalysis, *ACS Appl. Mater. Interfaces* 13 (2021) 2788–2798.
- [53] M.S.A. Akbari, R. Bagheri, Z. Song, M.M. Najafpour, Oxygen-evolution reaction by nickel/nickel oxide interface in the presence of ferrate(VI), *Sci. Rep.* 10 (2020) 8757.
- [54] S. Li, C. Xi, Y.-Z. Jin, D. Wu, J.-Q. Wang, T. Liu, H.-B. Wang, C.-K. Dong, H. Liu, S. A. Kulnich, X.-W. Du, Ir–O–V catalytic group in Ir-doped NiV(OH)<sub>2</sub> for overall water splitting, *ACS Energy Lett.* 4 (2019) 1823–1829.
- [55] A.P. Grosvenor, M.C. Biesinger, R.St.C. Smart, N.S. McIntyre, New interpretations of XPS spectra of nickel metal and oxides, *Surf. Sci.* 600 (2006) 1771–1779.
- [56] M. Fingerle, S. Tengeler, W. Calvet, T. Mayer, W. Jaegermann, Water interaction with sputter-deposited nickel oxide on n-Si photoanode: cryo photoelectron spectroscopy on adsorbed water in the frozen electrolyte approach, *J. Electrochem. Soc.* 165 (2018) 3148–3153.
- [57] J. Choi, D. Kim, W. Zheng, B. Yan, Y. Li, L.Y.S. Lee, Y. Piao, Interface engineered NiFe<sub>2</sub>O<sub>4–x</sub>/NiMoO<sub>4</sub> nanowire arrays for electrochemical oxygen evolution, *Appl. Catal. B–Environ.* 286 (2021), 119857.
- [58] K. Zhang, X. Xia, S. Deng, Y. Zhong, D. Xie, G. Pan, J. Wu, Q. Liu, X. Wang, J. Tu, Nitrogen-doped sponge Ni fibers as highly efficient electrocatalysts for oxygen evolution reaction, *Nano-Micro Lett.* 11 (2019) 21.
- [59] M. Han, J. Huang, S. Liang, L. Shan, X. Xie, Z. Yi, Y. Wang, S. Guo, J. Zhou, Oxygen defects in β-MnO<sub>2</sub> enabling high-performance rechargeable aqueous zinc/manganese dioxide battery, *iScience* 23 (2020), 100797.
- [60] N. Weidler, J. Schuch, F. Knaus, P. Stenner, S. Hoch, A. Maljusch, R. Schafer, B. Kaiser, W. Jaegermann, X-ray photoelectron spectroscopic investigation of plasma-enhanced chemical vapor deposited NiO<sub>x</sub>, NiO<sub>x</sub>(OH)<sub>y</sub>, and CoNiO<sub>x</sub>(OH)<sub>y</sub>: influence of the chemical composition on the catalytic activity for the oxygen evolution reaction, *J. Phys. Chem. C* 121 (2017), 6455–6423.
- [61] G. Cheng, T. Kou, J. Zhang, C. Si, H. Gao, Z. Zhang, O<sub>2</sub><sup>2–</sup>/O<sup>–</sup> functionalized oxygen-deficient Co<sub>3</sub>O<sub>4</sub> nanorods as high performance supercapacitor electrodes and electrocatalysts towards water splitting, *Nano Energy* 38 (2017) 155–166.
- [62] X. Wang, J. Sunarso, Q. Lu, Z. Zhou, J. Dai, D. Guan, W. Zhou, Z. Shao, High-performance platinum–perovskite composite bifunctional oxygen electrocatalyst for rechargeable Zn–air battery, *Adv. Energy Mater.* 10 (2019), 1903271.
- [63] X. Wang, S. Liu, H. Zhang, S. Zhang, G. Meng, Q. Liu, Z. Sun, J. Luo, X. Liu, Polycrystalline SnS<sub>x</sub> nanofilm enables CO<sub>2</sub> electroreduction to formate with high current density, *Chem. Commun.* 58 (2022) 7654–7657.
- [64] G. Meng, T. Wei, W. Liu, W. Li, S. Zhang, W. Liu, Q. Liu, H. Bao, J. Luog, X. Liu, NiFe layered double hydroxide nanosheet array for high-efficiency electrocatalytic reduction of nitric oxide to ammonia, *Chem. Commun.* 58 (2022) 8097–8100.
- [65] G. Meng, M. Jin, T. Wei, Q. Liu, S. Zhang, X. Peng, J. Luo, X. Liu, MoC nanocrystals confined in N-doped carbon nanosheets toward highly selective electrocatalytic nitric oxide reduction to ammonia, *Nano Res* 15 (2022) 8890–8896.
- [66] Y. Zhang, Y. Qiu, Y. Wang, B. Li, Y. Zhang, Z. Ma, S. Liu, Coaxial Ni–S@N-doped carbon nanofibers derived hierarchical electrodes for efficient H<sub>2</sub> production via urea electrolysis, *ACS Appl. Mater. Interfaces* 13 (2021) 3937–3948.
- [67] P. Peng, L. Shi, F. Huo, C. Mi, X. Wu, S. Zhang, X. Xiang, A pyrolysis-free path toward superiorly catalytic nitrogen-coordinated single atom, *Sci. Adv.* 5 (2019) 2322.
- [68] Z. Li, Y. Zhang, Y. Feng, C.-Qi Cheng, K.-W. Qiu, C.-Ku Dong, H. Liu, X.-W. Du, Co<sub>3</sub>O<sub>4</sub> nanoparticles with ultrasmall size and abundant oxygen vacancies for boosting oxygen involved reactions, *Adv. Funct. Mater.* 29 (2019), 1903444.
- [69] D.F. Abbott, D. Lebedev, K. Waltar, M. Povia, M. Nachtegaal, E. Fabbri, C. Copéret, T.J. Schmidt, Iridium oxide for the oxygen evolution reaction: correlation between particle size, morphology, and the surface hydroxo layer from operando XAS, *Chem. Mater.* 28 (2016) 6591–6604.
- [70] Q. Wang, X. Huang, Z.L. Zhao, M. Wang, B. Xiang, J. Li, Z. Feng, H. Xu, M. Gu, Ultrahigh-loading of Ir single atoms on NiO matrix to dramatically enhance oxygen evolution reaction, *J. Am. Chem. Soc.* 142 (2020) 7425–7433.
- [71] Z. Li, G. Jiang, Y.-P. Deng, G. Liu, D. Ren, Z. Zhang, J. Zhu, R. Gao, Y. Jiang, D. Luo, Y. Fei Zhu, D.-H. Liu, A.M. Jauhar, H. Jin, Y. Hu, S. Wang, Z. Chen, Deep-breathing honeycomb-like Co–N<sub>x</sub>–C nanopolyhedron bifunctional oxygen electrocatalysts for rechargeable Zn–air batteries, *iScience* 23 (2020), 101404.
- [72] X. Liu, W. Liu, M. Ko, M. Park, M.G. Kim, P. Oh, S. Chae, S. Park, A. Casimir, G. Wu, J. Cho, Metal (Ni, Co)–metal oxides/graphene nanocomposites as multifunctional electrocatalysts, *Adv. Funct. Mater.* 25 (2015) 5799–5808.
- [73] D. Wang, Q. Li, C. Han, Z. Xing, X. Yang, When NiO@Ni meets WS<sub>2</sub> nanosheet array: a highly efficient and ultrastable electrocatalyst for overall water splitting, *ACS Cent. Sci.* 4 (2018) 112–119.
- [74] H. Lee, S.B. Lim, J.Y. Kim, M. Jeong, Y.J. Park, W.-S. Yoon, Characterization and control of irreversible reaction in Li-rich cathode during the initial charge process, *ACS Appl. Mater. Interfaces* 10 (2018) 10804–10818.
- [75] J. Huang, J. Han, T. Wu, K. Feng, T. Yao, X. Wang, S. Liu, J. Zhong, Z. Zhang, Y. Zhang, B. Song, Boosting the hydrogen transfer during volmer reaction at oxides/metal nanocomposites for efficient alkaline hydrogen evolution, *ACS Energy Lett.* 4 (2019) 3002–3010.
- [76] Y. Jiang, Y.-P. Deng, R. Liang, J. Fu, R. Gao, D. Luo, Z. Bai, Y. Hu, A. Yu, Z. Chen, d-Orbital steered active sites through ligand editing on heterometal imidazole frameworks for rechargeable zinc–air battery, *Nat. Commun.* 11 (2020) 5858.
- [77] X. Han, X. Ling, D. Yu, D. Xie, L. Li, S. Peng, C. Zhong, N. Zhao, Y. Deng, W. Hu, Atomically dispersed binary Co–Ni sites in nitrogen-doped hollow carbon nanocubes for reversible oxygen reduction and evolution, *Adv. Mater.* 31 (2019), 1905622.
- [78] Y. Kim, D. Kim, R. Blum, G. Vardar, I. Waluyo, A. Hunt, J.T. Wright, J. P. Katsoudas, B. Yildiz, Thermally driven interfacial degradation between Li<sub>7</sub>La<sub>3</sub>Zr<sub>2</sub>O<sub>12</sub> electrolyte and LiNi<sub>0.6</sub>Mn<sub>0.2</sub>Co<sub>0.2</sub>O<sub>2</sub> cathode, *Chem. Mater.* 32 (2020) 9531–9541.
- [79] F. Frati, M.O.J.Y. Hunault, F.M.F. de Groot, Oxygen K-edge X-ray absorption spectra, *Chem. Rev.* 120 (2020) 4056–4110.
- [80] A. Badreldin, A.E. Abusraf, A. A-Wahab, Oxygen-deficient cobalt-based oxides for electrocatalytic water splitting, *ChemSusChem* 14 (2021) 10–32.
- [81] D. Wanga, Y.-P. Deng, Y. Zhanga, Y. Zhao, G. Zhou, L. Shui, Y. Hu, M. Shakouri, X. Wanga, Z. Chen, Defect engineering on three-dimensionally ordered macroporous phosphorus doped Co<sub>3</sub>O<sub>4–δ</sub> microspheres as an efficient bifunctional electrocatalyst for Zn–air batteries, *Energy Storage Mater.* 41 (2021) 427–435.
- [82] X. Han, X. Wu, C. Zhong, Y. Deng, N. Zhao, W. Hu, NiCo<sub>2</sub>S<sub>4</sub> nanocrystals anchored on nitrogen-doped carbon nanotubes as a highly efficient bifunctional electrocatalyst for rechargeable zinc–air batteries, *Nano Energy* 31 (2017) 541–550.